1-1-2015

Specialized Inter-Particle Interaction Lbm For Patterned Superhydrophobic Surfaces

Amal Saeed Yagub
Wayne State University,

Recommended Citation

Yagub, Amal Saeed, "Specialized Inter-Particle Interaction Lbm For Patterned Superhydrophobic Surfaces" (2015). *Wayne State University Dissertations*. 1388.
https://digitalcommons.wayne.edu/oa_dissertations/1388

SPECIALIZED INTER-PARTICLE INTERACTION LBM FOR PATTERNED SUPERHYDROPHOBIC SURFACES

by

AMAL YAGUB

DISSERTATION

Submitted to the Graduate School

of Wayne State University,

Detroit, Michigan

in partial fulfillment of the requirements for the degree of

DOCTOR OF PHILOSOPHY

2015

MAJOR: MECHANICAL ENGINEERING

Approved By:

(Advisor) Date

(Co-Advisor)

DEDICATION

This work is dedicated to my mother for her kindness and support, Thank you.

ACKNOWLEDGMENTS

I would like to express my appreciation to Prof. Trilochan Singh and Dr. Hassan Farhat for the important role they played during my PHD Studies.

I would like to thank Prof. Bryzik, Walter, Prof. Naeim Henein, Dr. Jansons, Marcis, and Prof. Eamon, Christopher for serving as my doctoral committee.

I would like to thank Dr. Sasidhar kondaraju for his reviews, comments and for providing a helping tools.

TABLE OF CONTENTS

LIST OF FIGURES

NOMENCLATURE

$f_i(x,t)$	Density distribution function
$f_i^{eq}(x,t)$	Equilibrium density distribution function
ξ	Macroscopic velocity
λ	The physical relaxation time
e_i	Lattice Link
c_i	Lattice velocity in the ith direction
δ_t	Lattice time step
δ_x	Lattice spacing
τ	Lattice relaxation time
ρ	Macroscopic density
ω_i	Weighting constant
Q	The number of lattice links of the used LBM scheme
C_s	Lattice speed of sound
P	Macroscopic pressure
ν	Kinematic viscosity
μ	Dynamic viscosity
u^{eq}	Macroscopic velocity
$F^{\sigma}(x,t)$	Fluid-Fluid Interaction force
$N^{\sigma}(x,t)$	Fluid-solid interaction
$E^{\sigma}(x,t)$	Gravitational Force

G	Green function
σ	Various mixture contributing components
$G_{\sigma\sigma'}$	Surface tension constant
G_{ads}^{σ}	The fluid-solid interaction strength
k	Interface curvature
γ_{LV}	The interfacial
γ_{SV}	vapor-solid tension
γ_{SL}	liquid-solid tension
A_{adh}	The adhesion force per unit length
$\cos\theta$	Static contact angle
R_f	The ratio of the actual area of the rough surface to the geometric projected area
φ_S	The remaining area fraction of the solid surface
f_{SL}	The fractional geometrical area of the solid-liquid under the droplet
θ_a	The apparent contact angle
θ^W	Wenzel's apparent contact angle
θ^C	Cassie's apparent contact angle
θ_{adv}	Advanced Angle

θ_{rec}	Receding Angle
θ_h	The contact angle Hysteresis
ΔP	Laplace pressure
P_D	Dynamic pressure
P_{WH}	Water hammer pressure
P_C	The capillary pressure
K	The droplet curvature
R_i	The initial drop radius
a	The pillar width
b	The pillars spacing
h	The pillars height
x_c	The critical capillary length
ζ	A dimensionless correction factor
lu	The Lattice unit of length
mu	The Lattice mass unit
B_o	Bond number
F	Source term

$\overline{U}$	Average velocity
R_e	The Reynolds number
$R_{e_{ch}}$	The channel Reynolds number
R_{e_d}	The droplet Reynolds number
H	The channel height
We	Weber number
U_o	The undisturbed centerline flow velocity
$\dot{\gamma}$	The shearing strain rate
q	The volumetric flow rate through the channel
P	The power required for moving the undisturbed flow through the channel
P_d	A droplet power number
w	Width of the channel
ℓ	The domain length
V_{dmc}	The velocity of the droplet mass center
$\forall_d$	The initial droplet volume
w_d	The drop width
$mgsin\alpha$	The downward component of drop volume

α	The slop angle
T	Dimensionless time step

CHAPTER 1

INTRODUCTION

1.1 Superhydrophobic Surface

Superhydrophobic surfaces are the subject of a wide range of research fields, because properties such as anti-sticking, anti-contamination and self-cleaning are useful. Superhydrophobic surfaces are desirable for many industrial and biological applications, for example, transparent and antireflective surfaces, fluidic drag reduction, battery and fuel cell application, enhanced water supporting force, controlled transportation of fluids, oil–water separation, self-cleaning windshields for vehicles, and the manufacture of water-proof and fire repellant clothing. Increasing the surface roughness for low surface energy materials is the main approach that has been developed to generate a superhydrophobic surface, and the contact angle CA is the main method to characterize the surface superhydrophobicity.

The surface wettability “the interaction between solid and fluid” is an intrinsic and important property; it is governed by the geometrical microstructure and the chemical structure of the surface. Wettability presents the ability of liquid wetting on a solid surface. This action is defined by the struggle between the cohesive forces of the liquid molecules among themselves and the adhesive forces, which result from the molecular interactions between the liquid and the solid. Strong adhesion and weak cohesion results in a high degree of wetting (a hydrophilic condition); conversely, weak adhesion and strong cohesion results in a high measured contact angles and poor wetting (hydrophobic conditions). The contact angle is an important parameter in wetting processes, because its measurement allows the evaluation of solid surface free energy. In other words, in the cases where the contact angle is low, more adhesion is present due to a larger surface area between the liquid and solid and results in higher surface energy.

There are two types of contact angles: for a flat surface, the static contact angle is obtained by sessile drop measurement, where the drop is deposited on the surface and the angle value is obtained. Dynamic contact angle is a non-equilibrium angle; it is measured during the growth and shrinkage of the water droplet. The difference between the growth angle (advancing angle θ_{adv}) and the shrinkage angle (receding angle θ_{rec}) is defined as contact angle hysteresis CAH ($\Delta\theta$).

Numerous studies define superhydrophobic surfaces as surfaces with water contact angles greater than 150°. But superhydrophobicity does not only mean a high contact angle, it has to be also a low contact angle hysteresis (< 10°) (Bhushan, Jung, & Koch, 2009), which is responsible the self-cleaning property.

1.2 Social and Economic Impact

Over the last decade, research on superhydrophobic surfaces has attracted a lot of interest because of their properties that are desirable and feasible for wide range of industrial and biological applications. This technology can bring great convenience into our daily lives, and due to their multiple advantages, superhydrophobic surfaces continue to receive more attention from research and development perspectives. Great number of publications was generated during the last decade. They aimed at identifying best theories, methods and procedures for designing superhydrophobic surfaces. . Fig (1) shows that the number of published articles on superhydrophobic surfaces between 2004 and 2014 grew by ~25 times the total number of those published previously This trend demonstrates a remarkable movement towards applying the accepted processes and characterization methods in several industrial fields.

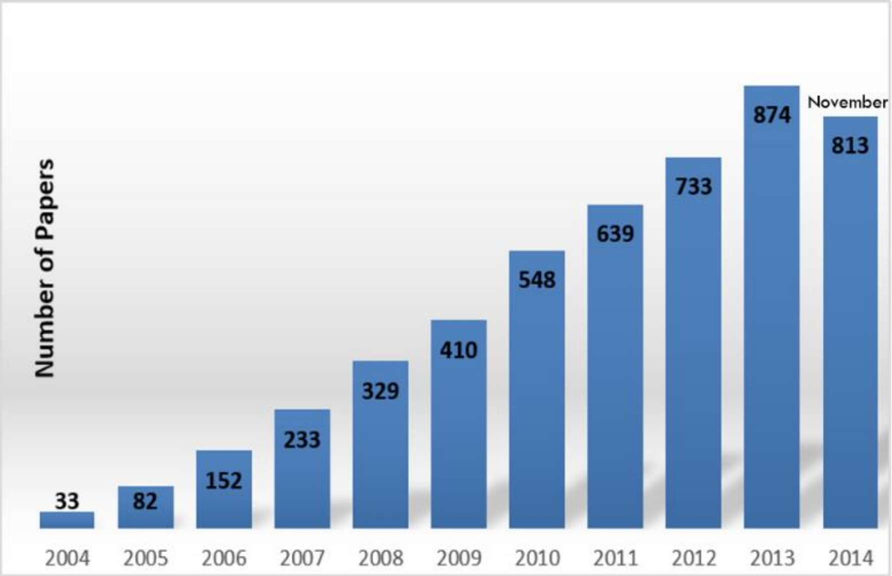

Fig 1.1- Number of papers published from 2004-2014 under the topic of superhydrophobic surfaces (Nagappan & Ha, 2015).

The applications of superhydrophobic surfaces are progressively increasing in several areas ranging from the textile to the military. These surfaces can be used in transparent and antireflective glass, submerged surfaces with reduced fluidic drag or floating with enhanced water supporting force, platform for controlled transportation of fluids, bio and anti-biofouling coating, filters for oil-water separation and manufacture of water-proof and fire retardant clothes.

Superhydrophobic surfaces can be used for solving snow related problems. Snow can build up on homes roofs or doorways causing significant damages. Snow can cause shortages in electrical insulators which results in ruining equipment and disrupting service. Snow buildup on aircraft wings and electrical transmission lines or towers can be dangerous and costly to repair. Since water droplets don’t stick to the superhydrophobic surfaces, the freezing droplets simply fall to the side. This feature enables superhydrophobic surfaces to be considered as a real solution for overcoming the above mentioned challenges.

Superhydrophobic surfaces stay clean; dirty liquids do not dry on the surfaces because dirt molecules cannot accumulate on these surfaces. Superhydrophobic coating can be applied in commonly used materials like beds and toilets to prevent spreading of disease-causing bacteria especially in hospitals. The property so called self-cleaning can be used for outdoor devices such as solar cell panels or satellite dishes. Antireflective superhydrophobic coating on solar cell surface can reduce the reflectance of the cell by 10% and provide a 17% increase in the output. Superhydrophobic coating decreases water uptake on the cell and help to maintain the antireflective performance(X. Zhang, Shi, Niu, Jiang, & Wang, 2008). Water repellency which reduces the interaction on solid-liquid interface can be used to reduce drag by moving the liquid in contact with the surface as in microfluidics, piping, and ship hull.

Superhydrophobic coatings have demonstrated improvement in corrosion prevention. Results for the cost of corrosion study (Davis, 2000); show that the total annual estimated direct cost of corrosion in the United States is $276 billion (~3.1% of the nation’s gross domestic product). For example, the number of ships serving U.S. ports includes more than 7000 ocean vessels, 737 vessels on the Great Lakes, and 122 cruise ships beside a huge number of recreational boats. The shipping industry cost of corrosion is $2.7 billion, broken down into new ship construction ($1.1 billion), maintenance and repairs ($0.8 billion), and corrosion-related downtime ($0.8 billion). Also, military’s equipment and facilities corrosion has been an enduring problem that is becoming more noticeable as the purchase of new equipment slows down. Corrosion is potentially the number one cost driver in lifecycle costs in industry – government sector (Projections to June 2013 indicate that total corrosion costs, direct and indirect, in the U.S. now exceed $1 trillion dollars or roughly 6% of GDP.). It is obvious, that enhancing our understanding of superhydrophobic surfaces can make them available to larger number of industrial products. This will create opportunities for tremendous cost saving on the national level.

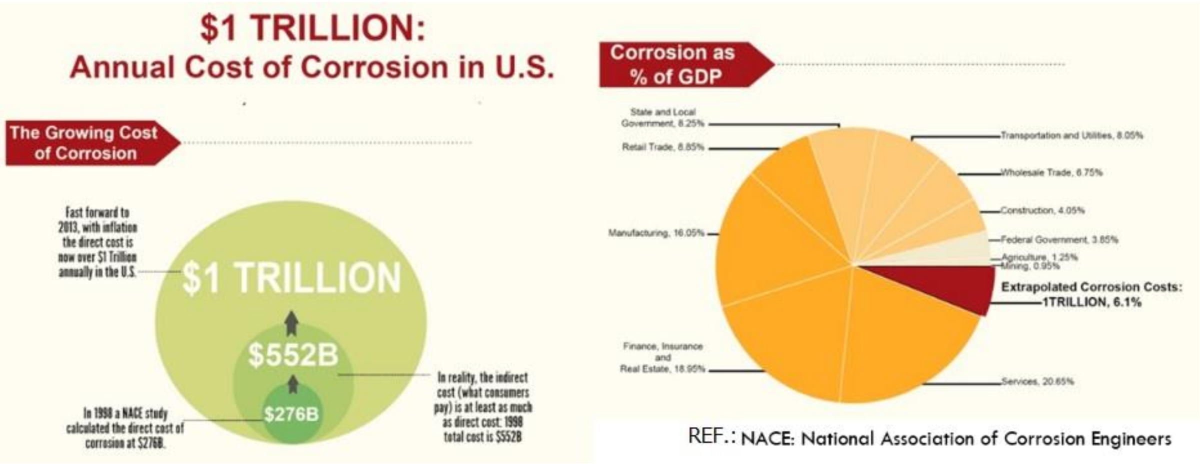

Fig 1.2 –Direct Cost of Corrosion in Industry Categories ($1.0 Trillion)

[Ref.:http://www.g2mtlabs.com/2011/06/nace-cost-of-corrosion-study-update/].

1.3 Numerical Methods for Superhydrophobic Surfaces Studies

Computational fluid dynamics (CFD) provides a good platform for the study of complex multi-phase and multi-component flows. The lattice Boltzmann (LB) approach is widely used to solve the equations of motion describing the dynamics of droplets on topologically patterned substrate. Several research works used tunable or controllable micro-structured superhydrophobic surfaces to study droplets movement on solid surfaces. The studies showed the possibilities of controlling the droplets motion to simulate some particular applications by using different source terms (Blossey, 2003; Feng & Jiang, 2006; Hong, Gao, & Jiang, 2007; Ma & Hill, 2006). Esmaili et al. (Esmaili, Moosavi, & Mazloomi, 2012) used a multi-component Shan-Chen lattice Boltzmann method (SC LBM) to study the dynamics of two dimensional (2D) droplets driven by under surface forces created by the chemical steps on the walls inside microchannels. They also, studied the effects of some parameters such as the height, wettability pattern, viscosity and the density ratio on the dynamics of the droplets under different conditions. Gong, and Cheng (Gong & Cheng, 2012), investigated the coalescence of droplets, which were driven by wettability gradients and the velocity field and mechanism of the droplet motion. (L. Hao & Cheng, 2009) simulated the dynamic behavior of the water droplet formation and removal in the micro-gas flow channel using the multiphase free-energy LBM approach. Their results showed that water droplets' removal is facilitated by a high gas flow velocity on a more hydrophobic gas diffusion layer (GDL) surface. (Huang, Shu, & Chew, 2008) studied the dynamics of droplets on chemical surfaces with different wettability patterns. They determined the effect of the frequency of wettability changes on the droplets positions and conditions. (Varnik, Dorner, & Raabe, 2007) investigated the effects of wettability and roughness gradient on the flow characteristics by using LBM and experimentally. A transition from laminar to unsteady flow was observed. This study showed the possibility to generate flow instabilities by a variation of the surface roughness at a Reynolds number for which the flow over a flat surface is laminar. (J. Zhang & Kwok, 2006) studied the motion of the contact line on topographic substrates. Their results showed that the dynamic contact angles change periodically between two maximum and minimum values and that the velocity is a function of the surface topology. (Vanapalli, Banpurkar, van den Ende, Duits, & Mugele, 2009) studied the effects of drop size, droplet viscosity and capillary number on the hydrodynamic resistance of a moving droplet confined in a rectangular microchannel by integrating a sensitive microfluidic comparator into a T-junction device and measuring the excess pressure drop.

Previous studies indicate that the SC model can be used for wide range of wetting studies in order to understand the effect of curved surfaces, droplet volume, surface wetting characteristics, wetting and de-wetting transitions and surfaces with different wetting characteristics. However, most of these studies involved flat surfaces or rough surfaces, which geometrical parameters (pillar size to droplet radius) did not warrant a realistic representation of the wetting state presented in most experimental works. The simulations performed on rough structured surfaces using SC model were only based on the studies involving a complete penetration of droplet into the rough surfaces.

This work shows that simulating realistic wetting conditions on rough surfaces with the SC model is rather more challenging. This is due to geometrical constraints which necessitate the use of 2D domains. Furthermore the challenges are due to the fact that the basic SC model lacks the capabilities of describing the underlying physics of the apparent contact angle on rough surfaces. This is caused by few inherent model effects, which prevent it from reproducing the right classical Wenzel and Cassie apparent contact angles.

The objective of this work is to provide a computational model which can be tuned to mimic the physical behavior of liquid droplets in contact with rough surfaces and predict their static and dynamic wetting characteristics.

CHAPTER 2

LITERATURE SURVEY

2.1 The lattice Boltzmann method

Computational fluid dynamics (CFD) provides a good platform for the study of complex multi-phase and multi-component flows. During the last couple decades, among many CFD tools, the Lattice Boltzmann Method (LBM) attracted more attention due to the simplicity of its algorithm, stability, and parallelism. Another advantage of the LBM is the no-slip bounce-back boundary condition, which allows the simulation of complex boundaries flows with little computational cost. LBM schemes have been applied in the study of wetting and spreading phenomena; among them is the Shan and Chen (SC) model, which is a good numerical tool for simulating multi-phase and multi-component flows. The SC's LBM is capable of handling multiphase fluids with density and viscosity difference. Shan and Chen introduced a nonlocal interaction potential approach that mimics the multiphase behavior. The SC method is easy to implement for simulating different multiphase problems, such as the droplet formation, breakup of a droplet, micro-droplet formation, and thermal multiphase flow.

2.2 LBM and the Shan and Chen Model:

The Lattice Boltzmann Model (LBM) has been used by many computational fluid researchers for studying variety of fluid problems in the last two decades. The single-relaxation Bhatnagar-Gross-Krook (BGK) is the most popular scheme among the isothermal Lattice Boltzmann equation (LBE) models. The LBGK uses the following equation for the collision and streaming steps(Yu, Mei, & Shyy, 2002):

$$\frac{df_i}{dt} + \xi_i . \nabla f_i = -\frac{1}{\lambda}(f_i - f_i^{eq}) \tag{2.1}$$

Where λ is the physical relaxation time, ξ is a macroscopic velocity, f^{eq} is an equilibrium distribution function, and f is a density distribution function. Equation (2.1) is discretized in space and time, which leads to:

$$f_i(\boldsymbol{x} + \boldsymbol{c}_i\delta_t, t + \delta_t) - f_i(\boldsymbol{x}, t) = -\frac{1}{\tau}[f_i(\boldsymbol{x}, t) - f_i^{eq}(\boldsymbol{x})] \tag{2.2}$$

where τ is the relaxation time, $\boldsymbol{c}_i = \boldsymbol{e}_i / \delta_t$ is the lattice velocity shown in Fig (2.2), f_i is a density distribution function, and the lattice spacing δ_x and the lattice time step δ_t. f_i^{eq} is an equilibrium distribution function in the i^{th} direction, is expressed as follows:

$$f_i^{eq} = \rho\omega_i[1 + \frac{3}{c^2}\boldsymbol{c}_i \cdot \boldsymbol{u}^{eq} + \frac{9}{2c^4}(\boldsymbol{c}_i \cdot \boldsymbol{u}^{eq})^2 - \frac{3}{2c^2}\boldsymbol{u}^{eq} \cdot \boldsymbol{u}^{eq}] \tag{2.3}$$

where $\boldsymbol{u}^{eq}$ and ρ are the macroscopic velocity and density, respectively, ω_i are weighting constants for the various lattice links:

- For D2Q9

$$\omega_i = [4/9; 1/36; 1/9; 1/36; 1/9; 1/36; 1/9; 1/36; 1/9]$$

-For D3Q19

$$\omega_i = [1/3; 1/36; 1/36; 1/18; 1/36; 1/36; 1/36; 1/18; 1/36; 1/18; 1/36; 1/36; 1/18; 1/36; 1/36; 1/36; 1/18; 1/36; 1/18]$$

where i indicate the lattice links shown in Fig. 2.1(Farhat, 2010), $\boldsymbol{u}^{eq}$ and ρ are the macroscopic velocity and density, respectively.

In the LBM, particle positions are confined to the nodes of the lattice; the variations in momenta, due to a continuum of velocity directions and magnitudes and varying particle mass, are reduced to: the simple 2-D model (8 directions, 3 magnitudes, and a single particle mass) this model is known as D2Q9, which describes 2 dimensional and contains 9 velocities, with the following end points coordinates:

e_0(0,0); e_1(-1,1); e_2(0,1); e_3(1,1); e_4(1,0); e_5(1,-1); e_6(0,-1), e_7(-1,-1,); e_8(-1,0)

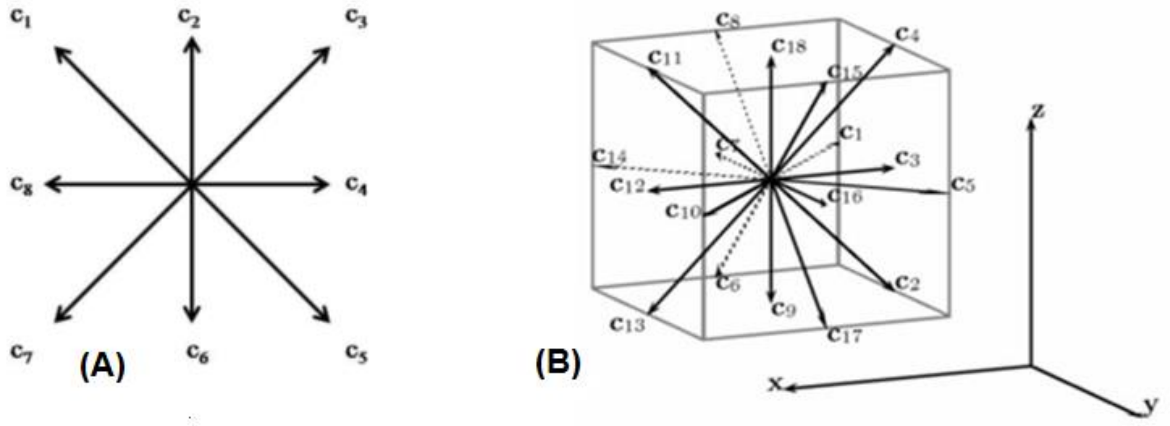

Fig. 2.1 - Lattice links for the: **(A)** - D2Q9 LBM, **(B)** - D3Q19 LBM.

and 3-D models known as D3Q19, and the lattice links have the following coordinates:e_0(0,0,0); e_1(-1,-1,0); e_2(-1,0,-1); e_3(-1,0,0); e_4(-1,0,1); e_5(-1,1,0); e_6(0,-1,-1), e_7(0,-1,0,); e_8(0,-1,1); e_9(0,0,-1); e_{10}(1,1,0); e_{11}(1,0,1); e_{12}(1,0,0); e_{13}(1,0,-1); e_{14}(1,-1,0); e_{15}(0,1,1); e_{16}(0,1,0); e_{17}(0,1,-1); e_{18}(0,0,1).

The speed of sound is $c_s = c/\sqrt{3}$. The kinematic viscosity is calculated using the relaxation time by:

$$\nu = (\tau - 0.5)c_s^2\delta_t \tag{2.4}$$

Among many LBM schemes, the Shan and Chen model is a model of choice for multiphase simulations. In the SC model, the density of the individual constituent fluids of the mixture and the composite macroscopic velocity is calculated using the density distributions functions of the fluids as follows:

$$\rho^{\sigma} = \sum_{i=0}^{Q-1} f_i^{\sigma} = \sum_{i=0}^{Q-1} f_i^{\sigma,eq}$$
$$\boldsymbol{u}^{'} = \frac{\sum_{\sigma} \frac{1}{\tau^{\sigma}} \sum_{i=1}^{Q-1} \boldsymbol{c}_i f_i^{\sigma}}{\sum_{\sigma} \frac{1}{\tau^{\sigma}} \rho^{\sigma}} \tag{2.5}$$

where σ refers to the various mixture contributing components, τ^{σ} is the individual component relaxation time from which different fluids viscosities can be derived using Equation (2.2). The fluid- fluid interaction force is represented by the following equation (Shan & Chen, 1993):

$$\boldsymbol{F}^{\sigma}(\boldsymbol{x},t) = -\rho^{\sigma}(\boldsymbol{x},t) \sum_{\sigma'} G_{\sigma\sigma'} \sum_{i=0}^{18} \omega_i \rho^{\sigma'}(\boldsymbol{x}+\boldsymbol{c}_i\delta_t, t)\boldsymbol{c}_i \tag{2.6}$$

where $\boldsymbol{F}^{\sigma}(\boldsymbol{x},t)$ is the interaction force exerted on component σ by the neighboring component σ' in the mixture. It is worth mentioning that the magnitude of this force which creates a pressure jump across the fluid-fluid interface is dependent on the constant $G_{\sigma\sigma'}$ and it determines the strength of the surface tension. The fluid-solid interaction force imposed by each fluid component is expressed as follows; (Martys & Chen, 1996):

$$\boldsymbol{N}^{\sigma}(\boldsymbol{x},t) = -\rho^{\sigma}(\boldsymbol{x},t) \sum_{i=0}^{18} \omega_i G_{ads}^{\sigma} S(\boldsymbol{x}+\boldsymbol{c}_i\delta_t)\boldsymbol{c}_i \tag{2.7}$$

where $S(\boldsymbol{x}+\boldsymbol{c}_i\delta_t)$ can only have a zero value for neighboring fluid node, and one for neighboring solid node respectively. G_{ads}^{σ} determines the interaction strength and it is positive for non-wetting fluid, and negative for wetting fluid. The force due to gravity is incorporated in the model through the following equation:

$$\boldsymbol{E}^{\sigma}(\boldsymbol{x},t)=\rho^{\sigma}(\boldsymbol{x},t)\boldsymbol{g} \tag{2.8}$$

where g is the gravitational constant. The collision step is calculated by:

$$\hat{f}_i^{\sigma}(\boldsymbol{x},t+\delta_t)=f_i^{\sigma}(\boldsymbol{x},t)-\frac{1}{\tau^{\sigma}}[f_i^{\sigma}(\boldsymbol{x},t)-f_i^{\sigma,eq}(\rho,\rho\boldsymbol{u}^{\sigma,eq})] \tag{2.9}$$

where $\hat{f}_i^{\sigma}$ refers to post-collision distribution functions for the various fluids, and τ^{σ} are their corresponding relaxation times. The equilibrium functions for the constituent fluids are calculated by Eq. (2.3) using the modified equilibrium velocities as proposed by Buick and Greated (Buick & Greated, 2000) to account for external forces:

$$\boldsymbol{u}^{\sigma,eq}=\boldsymbol{u}^{'}+\frac{\tau^{\sigma}(\boldsymbol{F}^{\sigma}+\boldsymbol{N}^{\sigma}+\boldsymbol{E}^{\sigma})}{\rho^{\sigma}} \tag{2.10}$$

To allow a density ratio up to 20, the equilibrium distribution functions are expressed as follows:

$$f_i^{\sigma,eq}=\rho\omega_i[r_i^{\sigma}+\frac{3}{c^2}\boldsymbol{c}_i\cdot\boldsymbol{u}^{\sigma,eq}+\frac{9}{2c^4}(\boldsymbol{c}_i\cdot\boldsymbol{u}^{\sigma,eq})^2-\frac{3}{2c^2}\boldsymbol{u}^{\sigma,eq}\cdot\boldsymbol{u}^{\sigma,eq}] \tag{2.11}$$

$$r_i^{\sigma}=\begin{cases}3-2\dfrac{\rho^{\sigma'}}{\rho^{\sigma}},\rightarrow i=0\\ \dfrac{\rho^{\sigma'}}{\rho^{\sigma}},\rightarrow i\neq 0\end{cases} \tag{2.12}$$

$$r_i^{\sigma'}=1,\rightarrow i\geq 0$$

where $\rho^{\sigma}, \rho^{\sigma'}$ are the heavy and the light fluid densities, respectively. The streaming step is executed for the various fluids using the following equation:

$$f_i^{\sigma}(\boldsymbol{x}+\boldsymbol{c}_i\delta_t, t+\delta_t) = \widehat{f}_i^{\sigma}(\boldsymbol{x}, t+\delta_t) \tag{2.13}$$

This is followed by calculating the macroscopic observables using Eq. (2.5).

LBM has been used in the study of fluid-solid interaction in micro-channels, on flat and rough surfaces. (Fei, Cheng, & Hong, 2006) studied the effect of the build-up of CO_2 bubbles generated at the Anode side on the performance of Micro-direct methanol fuel cells. The SC multiphase and multi-component model was used to optimize the cell reaction layer pore size with and without micro-pump and to study the effects of hydrophobicity of the walls. (van Kats & Egberts, 1998) used a three-phase (2D) lattice–Boltzmann model to simulate fluid–fluid interface at the microscopic scale. Florian et al. studied different spreading regimes of a droplet on a fluid–fluid interface depending on the dominating forces and both inertia and viscous resistance were induced. They found that the spreading rates derived from simulations agreed with analytically obtained spreading rates for both capillary- and gravity-driven flow. (Raiskinmäki, Koponen, Merikoski, & Timonen, 2000) simulated spreading of small droplets on smooth and rough solid surfaces using the three-dimensional LBM and found that this method can indeed be very useful in such studies. (Leopoldes, Dupuis, Bucknall, & Yeomans, 2003) studied the behavior of micron-scale fluid droplets jetted onto surfaces patterned with lyophobic and lyophilic stripes. Their results showed close quantitative correspondence between numerical solutions of the hydrodynamic equations of motion describing the spreading and the experimental results. Léopoldés et al. underlined the inherent difficulties in controlling the details of the formed patterns using inkjet printing and the subtle effects of the surface wetting properties on the behavior of liquids on patterned substrates. (Mo, Liu, & Kwok, 2005) employed the reactive-wetting technique by using the LBM to move liquid against gravitational force and studied the mass flow of the drop. Their results indicated that the method employed was suitable for producing most of the experimentally observable responses. (Kang, Zhang, & Chen, 2005) presented the dynamic behavior of a 3D immiscible droplet in a duct by the LB multiphase multi-component model to study the effects of the contact angle and capillary number on the droplet dynamics. The results pointed out that there exists a critical capillary number, under which the droplet would move along the wall and reach a steady state. To obtain a comprehensive understanding for the superhydrophobic surfaces, LBM is used as a suitable scheme to study the multiphase flows over surfaces with different structures. The LBM can recover correct macroscopic fluid motion by incorporating the complicated physics into simplified microscopic kinetic equations. (Y. H. Kim, Choi, & Lee, 2011) presented a LBM to provide a relationship between roughness and contact angle for superhydrophobic surfaces with different pillar shapes. They showed that the transition in the drop energy state corresponded to the point that the system had enough energy to overcome the energy barrier between its initial metastable composite state and the thermodynamically favored wetted regime. (Schmieschek & Harting, 2009) studied the dependence of the contact angle on some geometrical measurements and model parameters such as the curvature, system size, initial droplet volume, coupling parameter and wetting parameter (pseudo density).They pointed that the dependence of contact angle on the model parameters is stronger than its dependence on the geometric measurements. The effect of surface topography on the contact angle hysteresis has been studied by (Hyväluoma, Koponen, Raiskinmäki, & Timonen, 2007)**.** By using LBM using the SC multiphase model, they simulated droplets sliding on an anisotropic surface. The study showed that the contact angle hysteresis decreased as the surface becomes more hydrophobic. Hyväluoma concluded that the contact angle hysteresis is a better parameter for the purpose of characterizing the superhydrophobicity. (Dupuis & Yeomans, 2006)**,** studied movement of a drop pushed gently by a constant force across a superhydrophobic surface by using a free energy LB. They found that there is an increase in velocity of about 50% as the number of posts is decreased to zero for suspended drops. (Stensholt & Øien, 2011) tested the ability of LBM-SC scheme to present how the droplet motion induced by surface tension. The model revealed a proportional relationship between the velocity of droplet and the surface tension gradient, the droplet's radius, and the inverse of the viscosity. (Sbragaglia, Benzi, Biferale, Succi, & Toschi, 2006) presented a multiphase flows LBM to describe the wetting and dewetting transition of fluids in the presence of complex geometries in micro and Nano-devices. The study concluded that the physics of the boundary conditions is quantitatively reproduced by modeling the fluid at mesoscopic level, and showed the possibility to design smart surfaces by combining geometry and hydrophobicity, with slippage properties that can be changed by a control parameter.

In order to understand the relation between the wettability of a surface and droplet spreading mechanism, various numerical models were developed. The numerical schemes involved in these models included continuum approach based models such as VOF studies used by (Gerardo Trapaga & Szekely, 1991) and (G Trapaga, Matthys, Valencia, & Szekely, 1992), Lagrangian finite-element methods used by (Fukai, Zhao, Poulikakos, Megaridis, & Miyatake, 1993) and (Fukai et al., 1995), level-set approach developed by(Zheng & Zhang, 2000), and Lattice-Boltzmann models (LBM) such as free energy approach used by (Dupuis & Yeomans, 2004), Inamuro model (Inamuro, Ogata, Tajima, & Konishi, 2004) used the projection method to resolve the large density difference. Then (Yan & Zu, 2007) and (Y. H. Kim et al., 2011) used it for modelling of interfacial transport phenomena of two-phase and complex flows, and the pseudo-potential based approach developed by(Shan & Chen, 1993). Though the sharp interface developed by the continuum approach based models has an advantage over diffuse interface based lattice Boltzmann models, the interface modeling and complex grid adaptability of continuum models made it difficult to handle the problems related to droplet wetting and droplet dynamics. The inherent interface forming mechanism of LBM along with the nonlocal interaction potential among the nearest-neighboring particles made the pseudo-potential LBM (Shan & Chen, 1993) a good numerical tool for simulating multi-phase and multi-component flows. The scheme was first proposed by Shan and Chen, and thus will be further referred to as Shan and Chen (SC) model in the present work. (Martys & Chen, 1996) improved the SC model further by projecting the original scheme from 4D FCHC into D3Q19 regular lattice, and added gravity and fluid-solid interaction forces to simulate multi-component flows in porous media.

2.3 Static Contact Angle Analysis:

The contact angle measures the ability of a liquid to spread when deposited on a planar solid surface. The solid-air and liquid-air interfaces come together to form static contact angle (θ). The contact angle can be defined as the angle at which the outline tangent of a liquid drop meets a solid surface. Depending on the value of the contact angle, surfaces are considered as hydrophobic with angle ($\theta > 90^o$) or hydrophilic with angle ($\theta < 90^o$). Superhydrophobic surfaces are surfaces with contact angles ($\theta > 150^o$) (De Gennes et al., 2004).

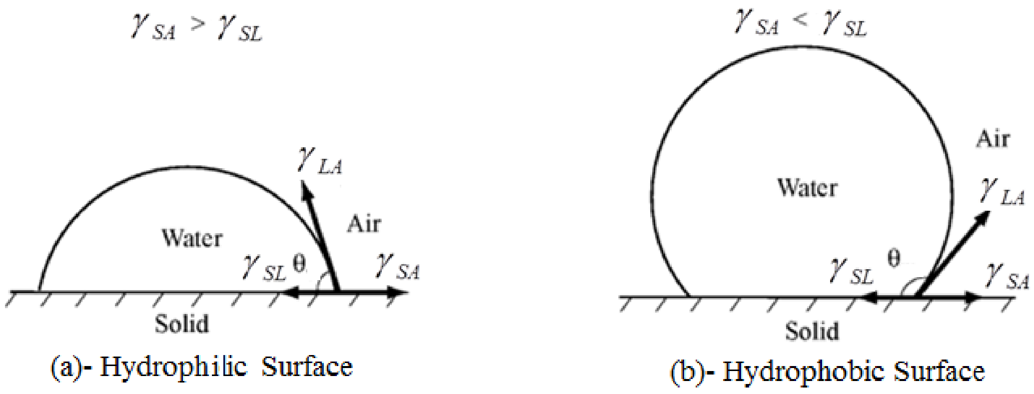

Fig 2.2 - Surface forces acting on the three phase contact line of a liquid droplet deposited on a substrate

There are several models for interface force equilibrium; the most general model is Laplace's theorem which indicates the relation between the surface tension and the pressure difference inside and outside of a spherical interface as (Okiishi, Munson, & Young, 2006):

$$\Delta P = 2\gamma / R \tag{2.14}$$

where, γ is a surface tension coefficient, R *is* radius of the interface.

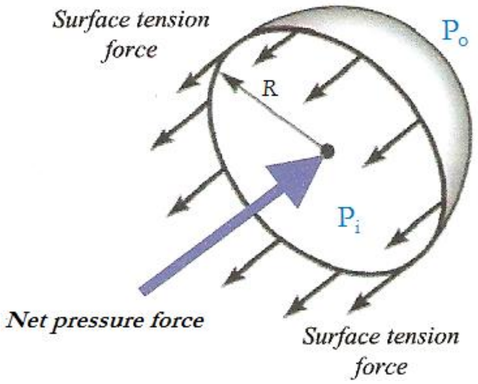

Fig 2.3– Liquid drop under zero-gravity (Michael Nosonovsky & Bhushan, 2005).

2.3.1 Smooth surface:

When a liquid contacts a solid surface, the molecular attraction reduces the energy of the system for the two separated surfaces. The work of adhesion per unit area between two surfaces is given by the Dupré equation (Bisanda, 2000):

$$W_{SL} = \gamma_{SA} + \gamma_{LA} - \gamma_{SL} \tag{2.15}$$

where γ_{SA} is the solid air surface tension, γ_{LA} is the interfacial tension and γ_{SL} is the solid liquid surface tension. The contact angle is determined from the condition of minimizing the total energy E_{tot} of the system. That is given by:

$$E_{tot} = \gamma_{LA}\left(A_{LA} + A_{SL}\right) - W_{SL}.dA_{SL} \tag{2.16}$$

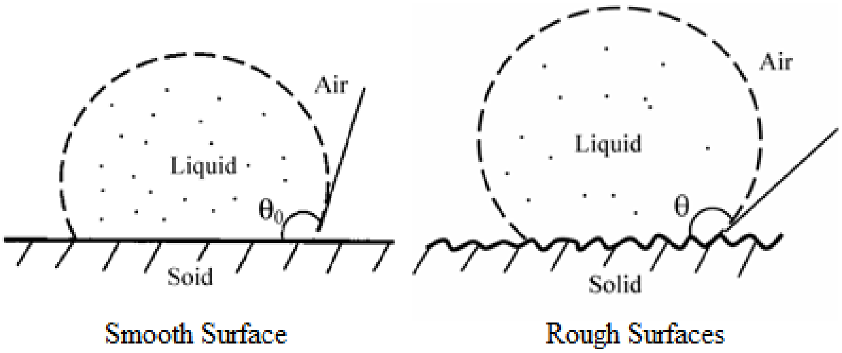

Fig 2.4 - Liquid droplet in contact with smooth and rough surfaces (Michael Nosonovsky & Bhushan, 2007).

By assuming that the droplet is small enough, so the gravitational potential energy can be neglected. At the equilibrium $dE_{tot} = 0$:

$$0 = \gamma_{LA}(dA_{LA} + dA_{SL}) - W_{SL}.dA_{SL} \tag{2.17}$$

For a droplet of constant volume, and using geometrical considerations:

$$\frac{dA_{LA}}{dA_{SL}} = \cos\theta_o \tag{2.18}$$

This leads to Young’s equation for the contact angle on flat surfaces (Michael Nosonovsky & Bhushan, 2007):

$$\cos\theta_o = \frac{\gamma_{SA} - \gamma_{SL}}{\gamma_{LA}} \tag{2.19}$$

Young’s expression is a simplification of the real situation and it is valid only for smooth homogeneous surfaces, which characteristics are not allowed to change due to interactions of the penetrating liquid with any outside force.

2.3.2 Rough surface:

To capture the effects of roughness (Wenzel, 1936) suggested the following changes to Eq. 2.18 with the assumption that the liquid is filling all the asperities:

$$\cos\theta = \frac{dA_{LA}}{dA_F} = \frac{A_{SL}}{A_F}\frac{dA_{LA}}{dA_{SL}} = R_f \cos\theta_o \tag{2.20}$$

where A_F is the projection of the rough surface and R_f is the surface roughness factor.

Wenzel State is valid only for moderate values of $R_f \left(-1 \le R_f \cos\theta_o \le 1\right)$. By considering a surface consisting of an array of high posts, the liquid cannot penetrate into the surface cavities, resulting in formation of air pockets. This leads to a composite solid–liquid–air interface as it was suggested by (Cassie & Baxter, 1944). The change in surface energy associated to a small displacement *ds* of the contact line, can be written as (José Bico, Thiele, & Quéré, 2002):

$$dE = \varphi_S(\gamma_{SL} - \gamma_{SA})\ ds + (1-\varphi_S)\ \gamma_{LA}\ ds + \gamma_{LA}\ ds\ cos\theta^* \tag{2.21}$$

$$0 = \frac{\varphi_S(\gamma_{SL} - \gamma_{SA})}{\gamma_{LA}} + (1-\varphi_S) + cos\theta^* \tag{2.22}$$

where θ^{*} is the apparent contact angle, $\varphi_S = R_f\ f_{SL}$ is the fraction of solid contacting the liquid and f_{SL} is the area fraction of the projected wet area. On rough surfaces if hypothetically only air was present between the solid and the liquid ($\varphi_S = 0$), the contact angle would be 180°. The apparent contact angle in the Cassie state θ^{C} is caused by both solid and air and this yields:

$$\cos\theta^{C} = -1 + \varphi_S\left(\cos\theta + 1\right) \tag{2.23}$$

For square topped pillar geometry (Milne & Amirfazli, 2012): $\varphi_s = a/c$, $1-\varphi_s = b/c$

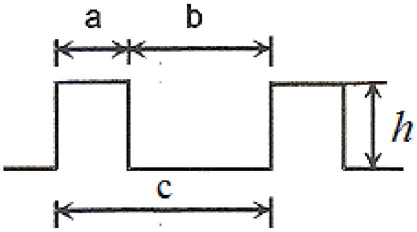

Fig 2.5- shows the view of roughness geometry of square pillars (Milne & Amirfazli, 2012).

Cassie-Baxter proposed a formulation for the composite interface apparent contact angle, based on subtracting the liquid-air differential area from the total area as follows:

$$\cos\theta = \frac{dA_{LA} - f_{LA}dA_{C}}{dA_{C}} = \frac{dA_{SL}dA_{F}dA_{LA}}{dA_{F}dA_{C}dA_{SL}} - f_{LA}$$

$$cos\theta = R_f\ \ f_{SL}\ cos\theta_o - 1 + f_{SL} \tag{2.24}$$

where A_C is the flat area of the composite interface and $f_{SL} = 1 - f_{LA}$ is the fractional flat geometrical area of the liquid-solid interface under the droplet.

The apparent contact angle is generally expected to follow the Wenzel behavior on surfaces with mild roughness and to obey the Cassie behavior on highly rough surfaces. Depositing a water droplet on a moderately $R_f \gg 1$ rough surface can lead to the Cassie-Baxter state with air pockets in the surface texture. In the CB state any addition of energy could lead to a transition to the Wenzel state. The contact angle resulting from a Wenzel shows increased sensitivity to contamination. On the contrary, for a Cassie-Baxter it would show decreased sensitivity. Physically, this explains that in Wenzel case, the liquid increases its contact with the solid, whereas in the Cassie-Baxter case the contact is decreased.

Numerous scientific papers have demonstrated how important roughness is for superhydrophobic surfaces and have focused on the relation between contact angles and surface geometry (Genzer & Efimenko, 2006; McHale, Shirtcliffe, Aqil, Perry, & Newton, 2004; Patankar, 2004a). It was of particular interest to understand which regime describes most accurately liquid wetting in the non-wettability regime. The Wenzel, Cassie and Cassie-Baxter formulas were used to explain the rough surfaces energetic. For square pillars of size ($a \times a$), height h, and spacing, arranged in a regular array, the Wenzel and Cassie apparent contact angles were calculated as follows (He et al., 2003):

$$cos\theta^{C} = A\,(1 + cos\theta_{o}) - 1 \tag{2.25}$$

$$cos\theta^{W} = \left[1 + \frac{4A}{a/h}\right] cos\theta_{o} \tag{2.26}$$

where $A = \dfrac{1}{\left(\dfrac{b}{a} + 1\right)^{2}}$

(He et al., 2003) showed experimentally that on same rough surface, there can be two contact angles corresponding to Wenzel's theory and Cassie theory. The droplet could have a composite or wetted state according to how it was formed. For instant the composite surface is formed and high contact angle obtained from gentle deposition of the droplet.

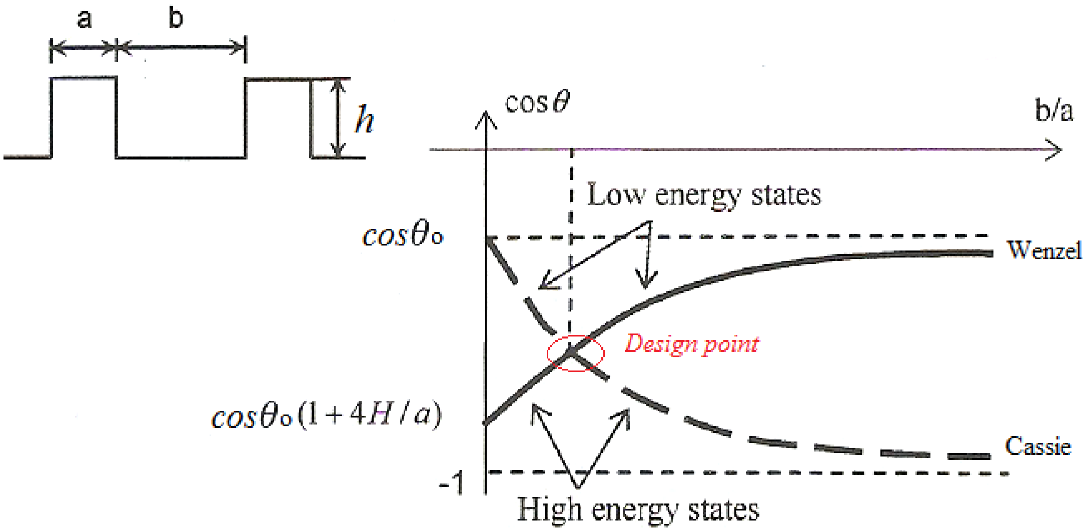

Fig 2.6 – The theoretical predicted apparent contact angle as a function of the geometric parameter (He et al., 2003).

The critical point, which is used to design a robust superhydrophobic, is the intersection point between the Wenzel and Cassie curves that shown in Fig (2.6). In this point, there is no change the CA even when transition from composite to a wetted surface occurs. The equilibrium contact angle θ_o as a function of geometric parameters at the critical point becomes:

$$cos\theta_o = \frac{1}{\left[\frac{4A}{(a/h)(A-1)} - 1\right]} \tag{2.27}$$

(Bhushan et al., 2009) studied the effect of micro, nano and hierarchical structures on superhydrophobicity, by analyzing the roughness factor and the static contact angle. They found that the roughness factor R_f and the fractional liquid-air interface f_{LA} of the hierarchical structure are higher than those for micro and nanostructures and the air present in hierarchical structure, decreases the solid-liquid contact area. (Bittoun & Marmur, 2009) studied the superhydrophobicity of different types of rough surfaces (cylinder, truncated cones, paraboloids, and hemispheres), by using theoretical model for Wenzel and Cassie-Baxter wetting states. They concluded that the surfaces which consist of paraboloidal protrusions are the optimal within the tested surfaces. (Patankar, 2009) investigated the drop energy on a solid surface with cavities and showed that the effective surface energy depends on the equilibrium state (stable or unstable) of liquid-air interface inside the cavities. He concluded that if the cavities are designed appropriately a high contact angle of a rough surface made of hydrophilic material can be reached it. (Michael Nosonovsky & Bhushan, 2005) studied the relationship between the local roughness and contact angle for various roughness distribution; they pointed out that for a surface with roughness induced superhydrophobicity, the asperities should be small compared to typical droplet size. The asperities should have high aspect ratio h/a to provide high surface area and should be tightly packed. This is to minimize the distance between them in order to avoid composite interface destabilization. The authors concluded that the hemispherically topped cylindrical and pyramidal asperities gave a maximum contact angle approaching 180°. The authors of (Martines et al., 2005; Yoshimitsu, Nakajima, Watanabe, & Hashimoto, 2002; Zhao, Park, & Law, 2012)studied the water wettability on surfaces comprising of pillars with different aspect ratios. By varying the aspect ratio of the pillars, through modifying the surface area of the pillars, they discovered that at low aspect ratios the wettability could be described by the Wenzel model. By increasing the aspect ratio there was a transition from the Wenzel to Cassie wettabilities. Other studies (Extrand, 2002; Marmur, 2003, 2004; Patankar, 2003) provided theoretical hypothesis for understanding wettability on rough surfaces by assuming an array of square pillars. They evaluated the wettability by using the Wenzel and Cassie models, and established the conditions for the existence of the Wenzel and Cassie regimes. These studies showed that in order to achieve non-wettable surfaces (Cassie regime); it is necessary to construct a surface from slender and sparsely spaced pillars. The wettability in the Wenzel and Cassie regimes was studied in detail in references (José Bico, Marzolin, & Quéré, 1999; J Bico, Tordeux, & Quéré, 2001; Lafuma & Quéré, 2003; Patankar, 2004b).The authors showed that there is a critical value of the roughness factor R_f above which the Wenzel regime is thermodynamically more stable and below which the Cassie regime exists. (Callies & Quéré, 2005) showed that metastable Cassie drops may form on surfaces, which thermodynamically prefer the Wenzel regime. The metastability was demonstrated in several ways, and that the state of the droplet depended on the amount of liquid as well as the means of depositing the liquid on the surface.

2.4 Dynamic Contact Angle:

Wenzel’s and Cassie-Baxter’s theories are widely used, but there is still continuing investigation about their applicability to dynamic droplet behavior. For a droplet moving along a solid surface, the droplet contact angle at the front (advancing angle) is greater than the back (receding angle), resulting in contact angle hysteresis. Contact angle hysteresis is an important parameter in understanding drop motion on a surface.

2.4.1 Furmidge expression for tilted surfaces:

When the droplet starts to slide, the gravity acting on the liquid drop becomes greater than the surface tension force, and contact angle hysteresis reaches its maximum value. The critical sliding angle (α) for the droplet can be calculated by balancing these two forces (Furmidge, 1962):

$$\gamma_{LV}(cos\theta_r - cos\theta_a) = \frac{mg}{w} sin\alpha \qquad (2.28)$$

where *m* is the droplet mass and *w* is the solid-liquid contact width. The critical line force *F* required for starting a drop movement over a solid surface is given by:

$$F = \pi\, b\, \gamma_{LA}(cos\theta_r - cos\theta_a) \qquad (2.29)$$

where b is the solid/liquid contact radius. By assuming that the center of mass of the droplet is lowered by a quantity δ, the surface tension force that tends to impose a minimal surface area, thus making the drop spherical, becomes $(\delta\, \gamma_{LA})$. Meanwhile the gravitational body force that tries to flatten the droplet is scaled as $(\rho g R^3)$.

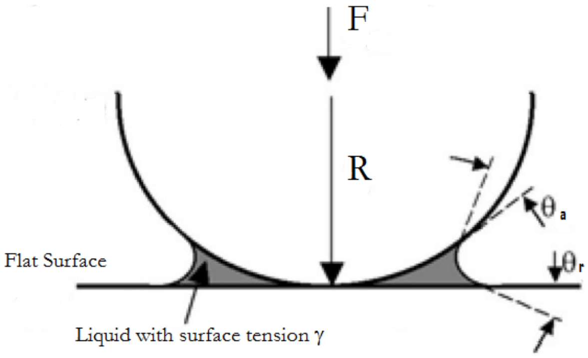

Fig 2.7 - Retention of liquid drops by solid surfaces (Furmidge, 1962).

The balance of these forces after considering the geometrical relation $b^2 \sim \delta . R$, yields (Quéré, 2008):

$$b = R^2\kappa \qquad (2.30)$$

κ is the capillary length $(\kappa = \sqrt{\gamma_{LA}/\rho g}) \sim 2.7mm$ for clean water at ambient conditions (S. H. Kim, 2008).

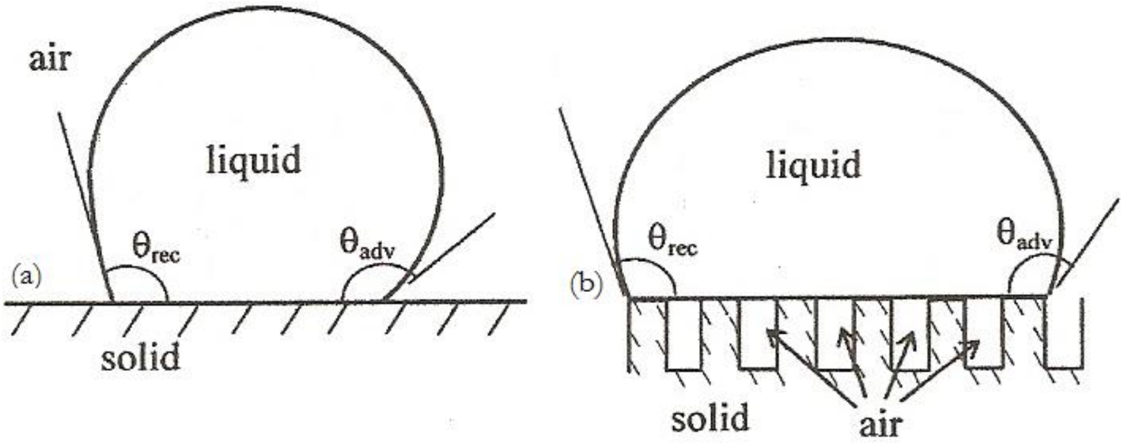

Fig 2.8- The values of advancing and receding contact angles for: (a) rough profile (b) rough profile with composite interface (Michael Nosonovsky & Bhushan, 2005).

The gravitational effect can be ignored when the liquid drop size is smaller than the capillary length (diameter < κ). The difference between the two angles $(\theta_a - \theta_r) = \Delta\theta_H$ is the contact-angle hysteresis.

2.4.2 Contact angle hysteresis:

It is not easy to obtain low contact angle hysteresis with low contact angle. It is also difficult to roll-off the droplet on the surface with low static contact angle except if the contact angle hysteresis is very small. The droplet can also roll-off with apparent contact angle that is larger than 150^o, even if the contact angle hysteresis is greater than 5^o. Wenzel state gives larger contact angle hysteresis than Cassie-Baxter state because as the contact line recedes the liquid fills the texture and eventually gets trapped in the surface (Harder, Shedd, & Colburn, 2008; Quéré, 2002). (Harder et al., 2008) showed that the contact angles increase in wetted area. Since the liquid penetrates the pattern in Wenzel regime, the wetted area increases with pattern depth. On the contrary, the contact angles in Cassie-Baxter regime depend on the proportion of the liquid solid interfacial area versus trapped air. This study concluded that the liquid has a physical interaction with the patterned base and the contact angles are independent of the pattern depth. (Raj, Enright, Zhu, Adera, & Wang, 2012) studied the droplet dynamics during the advancing, pinning and receding modes. Their results showed that heterogeneous surface plays a role in the contact line dynamics. They stated that for a low energy surface with high energy defects, the advancing contact angle was independent of the defect fraction and it had the same value as that of the homogeneous low energy surface. On the other hand, the receding angle was shown to be dependent on the relative fraction of the contact line on the respective surfaces, and it was influenced by the contact line distortion. (Gao & McCarthy, 2006) studied the droplet movement and repellency by (viewing) the contact line structure and energy barriers to contact line movement. They found that along the three-phase contact line, the droplet needed to either advance or recede to move. Change in the droplet shape (sphere) was required before it started to move. Sphericity was regarded as an activation barrier to motion that can be quantified by the increase in liquid/vapor interface area $\gamma_{LV} dA_{LV}$. Lichao G. and Thomas J. also showed that molecular level topography and flexibility impacted the contact angle hysteresis. (McHale, Shirtcliffe, & Newton, 2004) used Wenzel and Cassie-Baxter concepts to predict how hysteresis on a flat, smooth material, is transformed for a created superhydrophobic surface. They concluded that, in Wenzel case, the liquid increases its contact with the solid, whereas in the Cassie-Baxter case, the contact is decreased. (Quéré, 2002) showed that a high contact angle and low hysteresis can result in a reduction in the force required to set a drop into motion. Due to the difference in forces per unit length which is function of the liquid-vapor surface tension (γ_{LV}), which results in a differing contact angles at two sides of the drop, when the upper angle reaches the receding angle θ_{rec} and the lower angle reaches the advancing angle θ_{adv}, the drop just begins to move. (Kamusewitz, Possart, & Paul, 1999) studied the influence of the roughness of paraffin wax surfaces on the static and dynamic contact angle hysteresis. They found that the advancing angle increases by the same amount as the receding decreases with growing roughness, which is related to higher asperities due to the barrier effect. In other words, the capillary depression of the solid surface is responsible for the increase of advancing and receding water contact angles. Kamusewitz et al. reported that the liquid, the solid, the surface profile, the temperature and the immersion speed, may influence the equality between dynamic and static contact angles. (Chen et al., 1999) pointed out that the contact angle hysteresis is more important to fully characterize wettability than the contact angle. They concluded that the term superhydrophobic should be reserved for surfaces upon which, drops move easily when these surfaces are horizontal or near-horizontal. (Öner & McCarthy, 2000) showed experimentally that the receding angle on rough surface is lower than the one observed on the corresponding smooth surface with the same chemical composition, while advancing angles were higher than those on smooth surfaces. (Extrand, 2006) reported that for surfaces with optimal repellency, the asperity size, shape, and spacing are important parameters to produce a suspension pressure, which will resist the applied external pressure, due to the liquid column or impinging drops. He pointed out that the most effective way to reduce contact angle hysteresis of a super repellent surface is to decrease the linear fraction of contact line on the asperities.

2.4.3 Micro-devices and micro channels:

The motion of single and multiphase fluids in microdevices is also an important research topic due to its usefulness in a wide range of important applications. The fluidic drag reduction phenomenon of water flows on superhydrophobic surfaces has been explained theoretically and demonstrated experimentally. (Watanabe, Udagawa, & Udagawa, 1999) studied the slip of Newtonian fluids in pipes from a fluid mechanics' macroscopic point of view. Their experimental results showed that the laminar drag reduction ratio was about 14 % and it increased with increasing viscosity. (Ou, Perot, & Rothstein, 2004) demonstrated the existence of laminar drag reduction in rectangular microchannels through measuring the pressure drop resulting from the flow of water. The impact of the surface topology on the drag reduction was explored to highlight that, the effectiveness of these surfaces had increased with increasing the roughness spacing and decreasing the channel height. Confocal surface metrology system was used in this experiment to measure the deflection of an air–water interface that was formed between microposts and supported by surface tension. This shear-free interface reduced the flow resistance by allowing the fluid to contact only a very small effective area of the silicon surface. The results showed that with shear-free boundary condition, the pressure drop reductions increased up to 40% and the apparent slip lengths was larger than 20µm. In fuel cell systems, the superhydrophobicity of carbon nanotubes can promote the water removal from the electrode by repelling the water produced during the electrode reaction (X. Zhang et al., 2008). (Li, Wang, Chen, Waje, & Yan, 2005) developed a simple and scalable filtration method by preparing superhydrophobic oriented carbon nanotubes as cathode catalyst. This configuration helped improving the efficiency of the fuel cell. (Lifton, Simon, & Frahm, 2005) developed a new battery architecture based on a nanostructured superhydrophobic material combined with electro-wetting. This approach facilitated the creation of a structural design, which makes it possible to keep the electrolyte and electrode separate from each other.

CHAPTER 3
OUTLINE OF THE PRESENT WORK

3.1 Research objectives

The objectives of this work is to provide an efficient LBM SC based CFD model, capable of solving complex problems related to droplets behavior on superhydrophobic surfaces. This will be achieved through the following steps:

a. **Code development**

- Extend the multi-component LBM SC model to conform it to the theory of Wenzel and Cassie energy states by introducing a correction factor to the interfacial tension inducing source term.

b**. Validation**

- The developed code should be tested and validated through comparison with other numerical, analytical and experimental results.

c**. Application**

- Use the presented model in optimizing the energy required for the flow of single droplet in bounded channel with parabolic flow.
- Use the presented model in studying the effects of pinning on the movement of a single droplet on sloped surfaces.

3.2 Dissertation organization

In **Chapter 4** It was observed that surfaces fabricated with nano/micro roughness can manipulate the droplet contact angle, thus providing an opportunity to control the droplet wetting characteristics. Although the Shan and Chen (SC) lattice Boltzmann model (LBM) is good for simulating droplets wettability due to its realistic nature of droplet contact angle (CA) prediction on flat surfaces; however the SC-LBM was not able to replicate the CA on rough surfaces because it lacked a real representation of the physics at work under these conditions. By using a correction factor to influence the interfacial tension around the rough surface hence mimicking the physical forces acting on the droplet at its contact lines, the experimentally confirmed Wenzel and Cassie states were replicated. Roughness structures with different spacing were used to validate the study using the classical Wenzel and Cassie equations. The present work highlights the strength and weakness of the SC model and attempts to qualitatively conform it to the fundamental physics, which causes a change in the droplet apparent contact angle, when placed on nano/micro structured surfaces.

Chapter 5: The Lattice Boltzmann method is used to analyze the movement of droplets in contact with flat horizontal surfaces under the influence of parabolic flow, with and without roughness. This work identifies the main factors, which influence the multiphase fluids transport in squared channels. Effects of dimensionless radius, Weber number, Reynolds number and static contact angles are evaluated by calculating the power required for moving single droplets in comparison to the power needed for moving the undisturbed flow in the channel. Guidelines for optimizing the design of such flow are presented.

Chapter 6: The sliding-rolling of droplets on sloped surfaces with and without roughness is numerically investigated. The Shan and Chen (SC) Lattice Boltzmann model (LBM) is used to analyze the effect of pinning on the movement of droplets placed on sloped surfaces. The model is checked for conformance with the Furmidge equation which applies to tilted unstructured surfaces. It is shown that a droplet sliding on a perfectly smooth surface requires very minimal slope angle and that pinning due to the inhomogeneous nature of manufactured smooth surfaces is the key factor in determining the minimal slope angle. The model is also used on sloped rough surfaces to check the effects of roughness on the movement of single droplets. The numerical outcomes are compared with published experimental results for validation and a dimensionless number is suggested for quantifying the degree of pinning needed to control the behavior of sliding droplets on sloped surfaces.

Chapter 7 Presents a summary of the research findings, and suggests some future recommendations.

CHAPTER 4

A LATTICE BOLTZMANN MODEL FOR SUBSTRATES WITH REGULARLY STRUCTURED SURFACES ROUGHNESS

It was observed that surfaces fabricated with nano/micro roughness can manipulate the droplet contact angle, thus providing an opportunity to control the droplet wetting characteristics. The Shan and Chen (SC) lattice Boltzmann model (LBM) is a good numerical platform which holds strong potentials to qualify for simulating droplets wettability. This is due to its realistic nature of droplet contact angle (CA) prediction on flat surfaces. But SC-LBM was not able to replicate the CA on rough surfaces because it lacks a real representation of the physics at work under these conditions. By using a correction factor to influence the interfacial tension around the rough surface hence mimicking the physical forces acting on the droplet at its contact lines, the experimentally confirmed Wenzel and Cassie states were replicated. Roughness structures with different spacing were used to validate the study using the classical Wenzel and Cassie equations. This part highlights the strength and weakness of the SC model and attempts to qualitatively conform it to the fundamental physics, which causes a change in the droplet apparent contact angle, when placed on nano/micro structured surfaces.

The contact angle measures the ability of a liquid to spread on a surface. When a droplet is deposited on a planar solid surface, the contact angle can be defined as the angle at which the outline tangent of a liquid drop meets a solid surface. Depending on the value of the contact angle, surface properties are determined as hydrophobic ($\theta > 90$ degrees) or hydrophilic ($\theta < 90$ degrees). Superhydrophobic surfaces are surfaces with contact angles higher than 150 degrees. The contact angle is determined from the condition of minimizing the total energy of the system $dE_{Tot} = 0$, which leads to Young's equation.

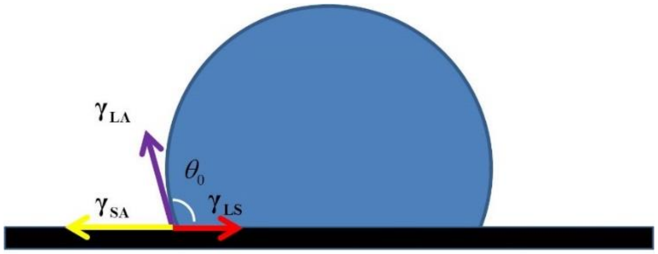

Fig. 4.1- Description of the forces per unit length acting on the contact line of a liquid droplet deposited on a flat surface at equilibrium

This chapter is organized as follows: section 4.1 reviews the LBM, the SC model, and provides a detailed description of the implementation of the effect of surface roughness in the SC model. Section 4.2 is a numerical simulation for the validation of the proposed model. Section 4.3 is the simulation results and discussion, and

4.1 Static Contact Angle in the Shan and Chen Model

In this chapter the LBM single-relaxation Bhatnagar-Gross- Krook (BGK) scheme, from section (2.2), is used for the simulation of contact angle problems.

For achieving static contact angle on a smooth flat surface in a physical system, Young's equation must be satisfied:

$$\gamma_{LV} \cos\theta = \gamma_{SV} - \gamma_{SL} \tag{4.1}$$

where γ_{LV}, γ_{SV} and γ_{SL} are the interfacial, vapor-solid and liquid-solid tensions, respectively. These are shown qualitatively in the left section of Fig. 4.2. The liquid-solid surface tension relation to the adhesion force per unit length is expressed by Dupré's equation (Giese & Van Oss, 2002):

$$\gamma_{SL} = \gamma_{LV} + \gamma_{SV} - A_{AD} \tag{4.2}$$

Substituting γ_{SL} in Eq. (18) yields the following relation between A_{AD} and γ_{VL}:

$$A_{AD} = \gamma_{LV}\left(1+\cos\theta\right) \tag{4.3}$$

Hence, the adhesion force determines the magnitude of the induced capillary force. The difference in strength between the liquid cohesive forces per unit length expressed through γ_{LV} and the adhesive forces per unit length A_{AD} determines the strength of the resulting liquid-solid surface tension γ_{LS} and thus the wetting characteristics leading to a droplet static contact angle. Larger the adhesion force is, the weaker the liquid-solid tension as per Eq. (4.2) and the smaller the static contact angle as per Eq. (4.3).

In the SC model Eq. (2.8) is used to control the contact angle of a droplet on a flat surface. This is shown in Fig. 4.2, where the phase field contours and velocity vectors indicate, that the contact angle can be controlled by tuning the values of the constants G_{ads}^{σ} for the suspending and suspended fluids. In the shown qualitative 2D simulation results of Fig. 4.2, the value of G_{ads}^{R} is negative, while G_{ads}^{B} varies from positive to negative. This change translates into a change in the wettability of the surface. An increase in the magnitude of the negative constant G_{ads}^{R} and a positive value of G_{ads}^{B} is observed to increase the wetting of the surface.

In the proposed model, the location of the adhesion forces application is within 2 nodes of the solid boundary. This is to apply the adhesion force below the center of the diffuse droplet interface.

Spreading of droplet in the numerical model is due to the vector addition of cohesive forces and adhesive forces at the triple point line. In the model, cohesive forces are controlled by a parameter $G_{\sigma\sigma'}$, and adhesive forces are controlled by a parameter G_{ads}^{σ} . The velocity vectors shown in Fig. 4.2, indicate that the resultant force acts outward on a wetting surface, and inward on a non-wetting surface. The achieved steady state contact angle depends mainly on the droplet local capillary number which magnitude determines the limits of droplet deformation. At the droplet base, the adhesion forces have their directions perpendicular to the solid surface, while the interfacial tension force, which presence is due to model spurious effects is normal to the interface. The addition of all forces changes the resultant direction at the droplet interface with the wall and gradually alters the droplet shape in the vicinity of the solid from spherical to flat.

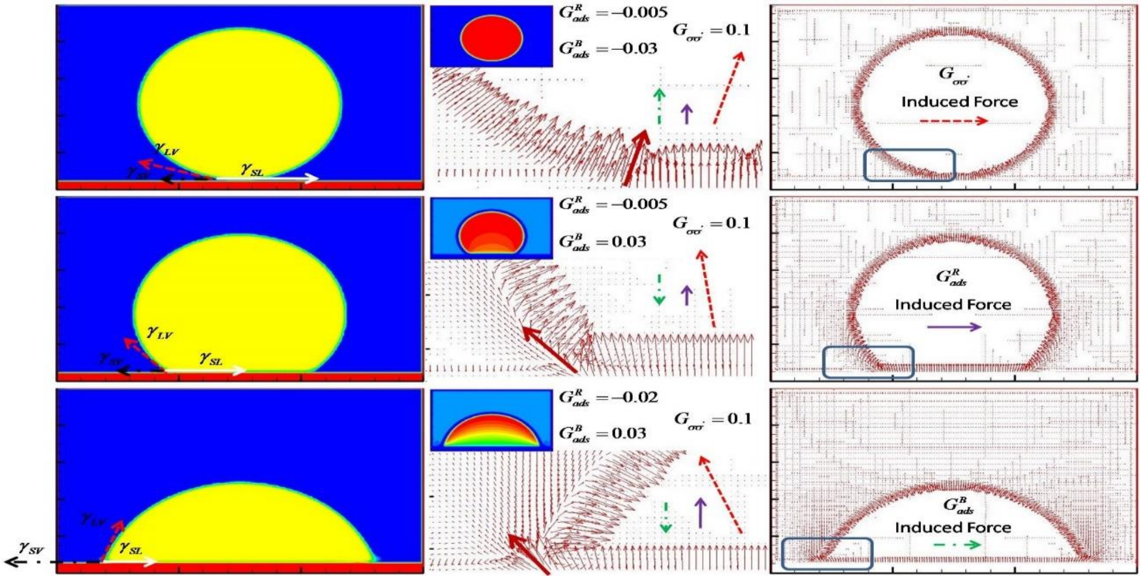

Fig. 4.2- Phase field and velocity vectors for droplets in close proximity to a flat surface. The qualitative magnified velocity vectors description shows that a resultant force acts in the vicinity of the contact line and determines the droplet behavior. The small insets in the picture are the pressure contours of the droplet for the different cases. The left side arrows are for conceptual explanation of the Young's equation for static contact angle.

The model behavior is in qualitative conformance with the theory of wetting. The effect of imposing positive constant G_{ads}^{B}, combined with increasing the magnitude of the negative constant G_{ads}^{R} in the model, i.e. increasing the liquid-solid adhesion force is similarly observed, to diminish the liquid-solid tension and thus leading to more droplet spreading and a decrease in the contact angle. This is obvious from the pressure contours of the three cases shown in Fig. 4.2, where lower pressure indicative of lower tension, is associated with lower contact angle.

The contact angle is usually used to quantify adhesiveness. In the cases where the contact angle is low, more adhesion is present. Strong adhesion and weak cohesion in water systems results in hydrophilic condition with low measured contact angles and high degree of wetting. Conversely, weak adhesion and strong cohesion results in hydrophobic conditions with high measured contact angles and poor wetting (Barnes & Gentle, 2011).

4.2 Apparent contact angle in the Shan and Chen Model

The effects of surface roughness on the static contact angle of a droplet can be explained by two main theories:

-Wenzel's theory assumes that the liquid fills the cavities of the rough substrate. The apparent contact angle θ^{w} due to the surface roughness is calculated with respect to the static contact angle on a flat surface θ by the following (Wenzel, 1936):

$$\cos\theta^{W} = R_f \cos\theta \tag{4.4}$$

where R_f is the ratio of the actual area of the rough surface to the geometric projected area.

-Cassie's theory assumes that air is trapped in the asperities of the rough surface and a composite surface is formed as shown in the right section of Fig. 4.3. The apparent contact angle is given by the following equation (Cassie & Baxter, 1944):

$$\cos\theta^{C} = -1 + \varphi_S \left(\cos\theta + 1\right) \tag{4.5}$$

where φ_S is he remaining area fraction of the solid surface.

Wenzel and Cassie equations are considered as special cases of what is known as the Cassie-Baxter equation. The Cassie-Baxter theory uses the following formula for calculating the apparent contact angle of a droplet deposited on a rough surface (Michael Nosonovsky & Bhushan, 2007):

$$\cos\theta^{CB} = R_f \, f_{SL} \cos\theta - 1 + f_{SL} \tag{4.6}$$

where f_{SL} is the fractional geometrical area of the solid-liquid under the droplet. From Eq. (4.6) it is obvious that Eq. (4.4) can be recovered if $f_{SL} = 1$. Equation (4.5) can as well be recovered from Eq. (4.6) if $R_f \approx 1$ and $f_{SL} = \varphi_S$.

In the presence of surface roughness in a physical system and depending on how the droplet is deposited on the surface, Wenzel's or Cassie's type of wetting could prevail. The composite surface could be maintained, or there could be a transition to completely wetted surface if external energy is added, such as dropping the droplet from a height or squeezing it against the surface roughness (He et al., 2003; Zhu, Feng, Ye, & Zhou, 2006).

A force balance at the interface within the asperities of a dynamic droplet, determines the state to which the droplet belongs. The interface is subjected to the following forces: Laplace pressure $P_{IN} - P_{OUT} = 2\gamma_{LV}K$ induced force, kinetic impact force resulting in dynamic pressure $P_D = \rho V^2 / 2$ and water hammer pressure $P_{WH} = k\rho VC$ resulting force due to the capillary waves during and shortly after impact (Kwon, Paxson, Varanasi, & Patankar, 2011). K is the droplet curvature, $\Delta P = P_{IN} - P_{OUT}$ is the pressure difference between the fluids inside and outside of the droplet, V is the velocity of the fallen droplet, k is a constant and C is the speed of sound. For a gently deposited small droplet it is obvious that the only force that is applicable to the interface is due to the Laplace pressure.

The forces on the inner side of the interface are counteracted upon by the capillary force which is a function of the interfacial tension and the specific geometry of the surface roughness. The capillary pressure induced by an array of square pillars, was calculated by (Patankar, 2010) as follows:

$$P_c = \frac{\gamma}{a}\left[\frac{-4\cos(\theta_a)}{A^{-1}-1}\right]; A = 1 \Big/ \left(\frac{b}{a}+1\right)^2 \qquad (4.7)$$

where γ is the surface tension of the liquid, θ_a is the advancing contact angle, a is the pillar width and b is the pillars spacing.

For static droplets, the height of the interface at a given distance *x* from the roughness peak, can be assessed by solving the following non-linear equation (Lister, Morrison, & Rallison, 2006):

$$\gamma_{LV}\frac{d^2h}{dx^2} = \left(-\Delta P + \Delta\rho gh\right)\left[1+\left(\frac{dh}{dx}\right)^2\right]^{\frac{3}{2}} \qquad (4.8)$$

where *h* is the height of the interface at a given distance *x*. The wetting state of the static droplet is pretty much determined by the height of the interface at the middle of the roughness spacing. A direct contact between the droplet interface with the base surface leads to total wetting of the surface.

Plotting Eq. (4.7) for several structured surfaces with a simulation value of the surface tension $\gamma = 3.5\times10^{-2}$, two advancing contact angles $\theta_a = 110^0$, $\theta_a = 75^0$ and several roughness spacing is shown in Fig. 4.3-A&B. This was done to qualitatively show a diminishing trend of the capillary pressure with the increase in the roughness' spacing for non-wetting angle and conversely an increasing trend for a wetting angle.

In the presence of structured surface in the SC numerical model, it is observed that for simulated droplets with static contact angle of 110 *degrees*, the effects of the capillary pressure increases with increasing the roughness' spacing for the same values of G_{ads}^{σ} as shown qualitatively by the droplet phase field contours in Fig. 4.3-A&B. Smaller spacing causes more impalement of the droplet and lower contact angle. Conversely larger spacing leads to composite wetting and higher contact angle. An estimation of the capillary pressure in the presented simulations of Fig. 4.3-C is achieved by rewriting Eq. (4.8) as follows:

$$P_c \approx \Delta\rho g h - \frac{\gamma_{LV}\dfrac{d^2h}{dx^2}}{\left[1+\left(\dfrac{dh}{dx}\right)^2\right]^{\frac{3}{2}}} \tag{4.9}$$

where $\Delta\rho$ is the density difference between the liquid and vapor across the interface, *g* is the acceleration due gravity and *h* is the height of the interface from the top of the rough surface. The heights of the interfaces of the four cases were measured directly from the simulations. To solve for the first and second derivatives of Eq. (4.9), parabolic shape was assumed for the interface within each of the asperities. The following parabolic equation was used for the solution:

$$h = ax^2 + b \tag{4.10}$$

The measured depth of the interface at the center was used to determine the coefficient *b* at *x* = 0 and the boundary condition *h* = 0 at *x* = *S*/2 (spacing midpoint) was used for determining the coefficient *a* in Eq. (4.10) for each case. This led to the simplification of Eq. (4.9) to the following:

$$P_c \approx \Delta\rho g\left(ax^2 + b\right) - \frac{\gamma_{LV}\, 2a}{\left[1 + \left(2ax\right)^2\right]^{\frac{3}{2}}} \tag{4.11}$$

The capillary pressure was calculated at several values of *x* throughout the spacing of each simulation case and averaged values were used for plotting the line graph shown in Fig. 4.3-C. As shown from the graphs for the capillary pressure and the droplets' phase field contours in Fig. 4.3, the behavior of the droplet on a structured surface in the standard SC model is in contradiction with the behavior of the physical systems described by Eq. (4.7). This behavior results from the local nature of the three forces induced by the constants $G_{\sigma\sigma'}, G_{ads}^{\sigma}$ and from the indifference of the numerical model to the length scale of the constituent geometry. The critical capillary length is calculated as follows:

$$x_c = \left(\frac{\gamma_{LV}}{\Delta\rho g}\right)^{\frac{1}{2}} \tag{4.12}$$

The capillary length which determines the application range of the capillary pressure in a structured surface is not considered in the standard SC model.

The apparent contact angle on structured surfaces in the SC model is affected mainly by the number of suspending fluid nodes within the asperities. Narrower roughness' spacing leads to higher pressure difference across the interface of the droplet, which when augmented by the influence of the adhesion force of the walls, drives the interface into the asperities; hence the SC model will always force Wenzel type of wetting for positive values of G_{ads}^{B} and negative values of G_{ads}^{R} in case of narrow structure spacing.

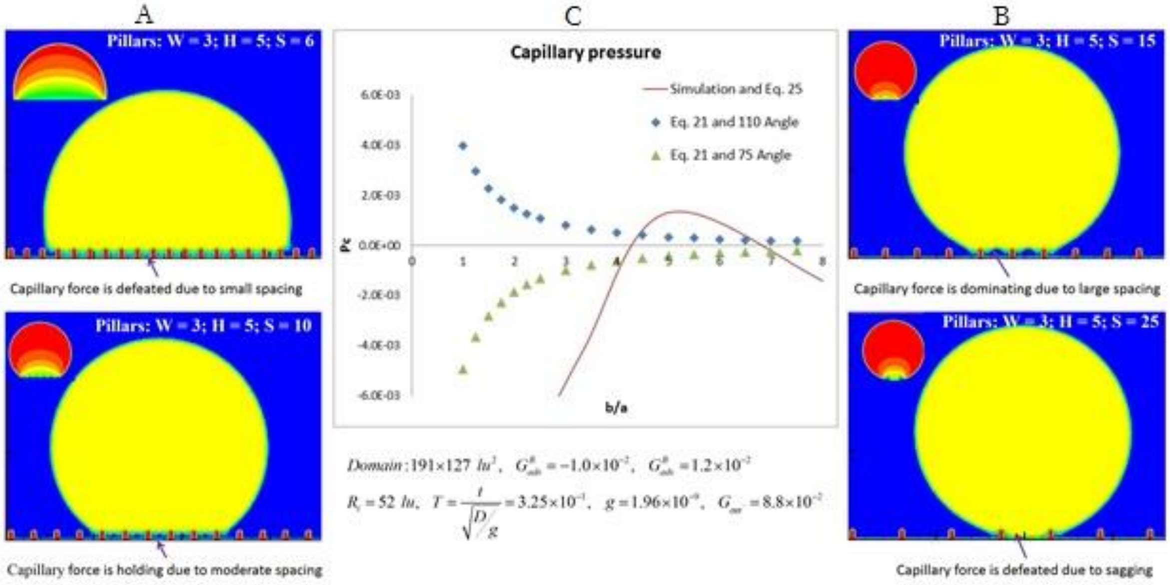

Fig. 4.3: **A** and **B**- Phase field contours for droplets deposited on four surfaces with different spacing and static contact angle of 110 *degrees*. The pressure contours shown as insets indicate the standard SC LBM trend of diminishing pressure inside the droplet at the surface contact location with smaller roughness spacing. **C**- Capillary pressure calculated by Eq. (4.7) in the presence of structured roughness for static angle 110 *degrees*, 75 *degrees* and width *a* = 3. The line curve is the Capillary pressure calculated by Eq. (4.11) with the interface height measured directly from the presented simulations.

Considering the contradicting behavior of the model with respect to the physical system described by Eq. (4.7), it is important to notice that at certain spacing the calculated capillary pressure (with diminishing trend for larger spacing and non-wetting angle) and the simulated capillary pressure (with increasing trend for larger spacing) intersects. This intersection is shown in the graphs of Fig. 3-C and is located between 4 < *b*/*a* < 5.

It is also worth noting that with larger spacing and due to the pressure difference between the inside and outside fluids of the droplet, sagging of the interface is witnessed in the standard SC model as shown in the last case in Fig. 4.3, although the apparent contact angle is large compared to the calculated angle by the Wenzel theory.

4.3 Correction factor for improving the apparent contact angle in the Shan and Chen model

A closer look at Eq. (4.8) reveals that the interface of a droplet will be concave upward for $P_B < P_R$ and concave downward for $P_B > P_R$. A structured surface is successful in efficiently repelling liquids if it has properties which can lead to an interface in a concave downward position, i.e. the surface will help retain the pressure of the vapor in the asperities relative to the inner droplet pressure. This can be executed through diminishing the local interfacial tension of the droplet in the vicinity of the surface structure.

In line with the logic presented above and to remedy the inherent SC based LBM model problems when simulating the Cassie, Cassie-Baxter and Wenzel conditions, the basic approach for the fluid-solid interaction is maintained by applying Eq. (2.7) to all fluid nodes above the rough boundary; however a correction to Eq. (2.7) is used for all fluid nodes inside the depression zones:

$$\boldsymbol{F}^{\sigma}(\boldsymbol{x},t)=\xi\rho^{\sigma}(\boldsymbol{x},t)\sum_{\sigma'}G_{\sigma\sigma'}\sum_{i=0}^{Q-1}\omega_i\rho^{\sigma'}(\boldsymbol{x}+\boldsymbol{c}_i\delta_t,t)\boldsymbol{c}_i \tag{4.13}$$

where $\xi=-1+f$ is a dimensionless correction factor, used to tune the wettability of the rough surface.

To test the proposed approach, several cases for simulating a droplet on a single structured surface with spacing *S* = 6 lattice units were used for investigating the effects of locally altering the interfacial tension within the asperities. The domain and simulation conditions were the same as in the previous cases shown in Fig. 4.3.

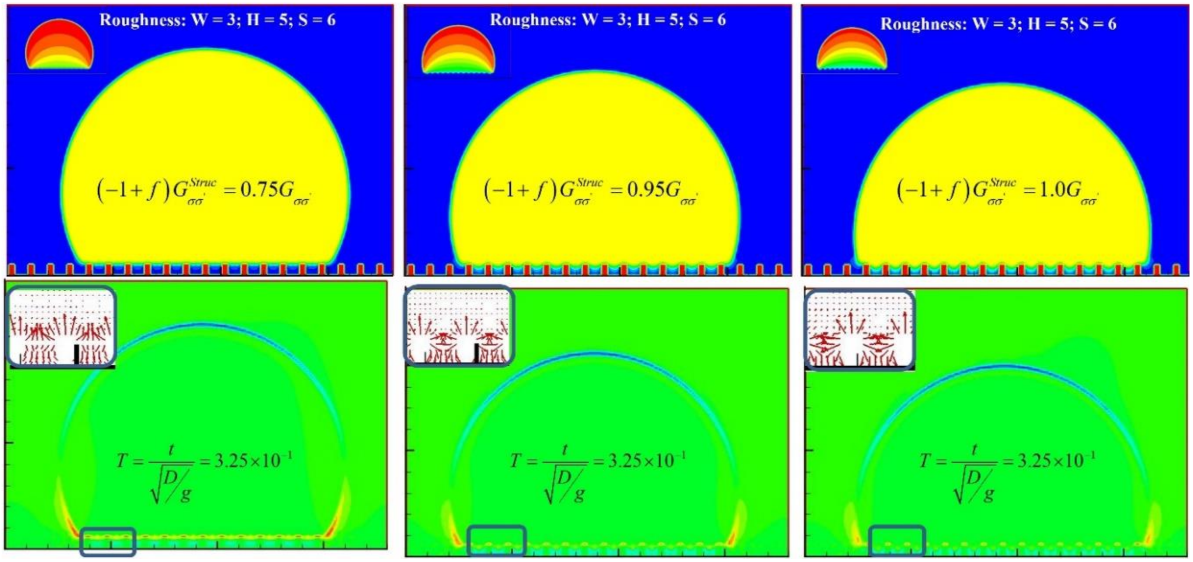

Fig. 4.4. Top – Phase field and pressure contours for droplets deposited on three surfaces with same roughness width and spacing but with altered SC LBM interfacial tension constant within the asperities for imposing a non-wetting droplet behavior. Top insets – Pressure contours for the three droplets with different correction constants. Bottom – Velocity contours in the vertical direction showing that with *f* = 0.25 the velocity in the vicinity of the roughness favors a non-wetting condition of the droplet. Bottom inset – Magnified velocity vectors around the structure showing the numerical effects of reducing the local interfacial tension within the asperities on the velocity magnitude and direction.

The results of three simulations are presented in Fig. 4.4, from which it is observed that by reducing the interfacial tension within the asperities, the wetting conditions of the droplet has transitioned from wetting to composite state. The velocity contours in the vertical direction are shown in the right section of Fig. 4.4, where it is obvious that for a correction constant *f* = +0.25 the velocity magnitude in the positive vertical direction is greater than those with constants *f* = +0.05 and *f* = 0. The inset in the right section of Fig. 4 zooms on the velocity vectors at the lower left corner of the droplet. These vectors show that by increasing the correction constant *f* in the positive range, the velocity magnitude has increased in the upward direction. This is indicative of a pressure balance across the interface which favors a concave downwards interface and hence a composite droplet wetting state.

Knowing that spacing characterized by 4 < *b*/*a* < 5 does not require any corrections as this was shown by the intersection of the capillary pressure curves in the graph of Fig. 4.3, a pivotal spacing can be used for determining the value of the correction constant *f* by scaling. The value of *f* is calculated by the following proposed scaling equation:

$$f = \frac{\left(\frac{\left(P_{c_{pivot}} - P_{c_{target}} \right)}{P_{c_{pivot}}} \frac{b_{pivot}}{b_{target}} \right)}{Q} \tag{4.14}$$

where $P_{c_{pivot}}$ and $P_{c_{target}}$ are the capillary pressures of the pivotal and the targeted spacing, respectively. These pressures are calculated using Eq. (4.7), where *b* is the spacing between the opposing peaks of the structured roughness and *Q* is the number of lattice links of the used LBM scheme.

From Eq. (4.13) the dimensionless correction constant *f* acts to increase the model capillary pressure for spacing below pivotal and to decrease the capillary pressure for spacing above pivotal. This is due to a change in sign of the constant *f* when moving from below to above pivotal spacing. Below pivotal spacing the constant is *f* > 0. This leads to $-1 < \xi < 0$ within the structured spacing and hence an increase in the capillary pressure through defeating the local interfacial tension. Conversely above the pivotal spacing the constant is *f* < 0. This leads to $\xi < -1$ within the structured spacing and hence a decrease in the capillary pressure through augmenting the local interfacial tension.

The condition for the application of the correction factor in the proposed model is dependent on the spacing between the rough surface peaks, which should be smaller than the critical capillary length x_c .

4.4 Implementation of the apparent static contact angle correction in the SC model for realistic droplets

A 2D domain consisting of $1400\ lu^2$ was used in the simulations. In this work ts is the lattice time step, mu is the lattice mass unit and lu is the lattice unit of length. The relaxation time was set to $\tau = 0.945$, resulting in a kinematic viscosity $\nu = 0.148\ lu^2/ts$. The density of the vapor was $\rho_B = 1 mu/lu^3$, while $\rho_R = 16 mu/lu^3$ was used for the liquid density. The fluid-fluid interaction constant was set to $G_{\sigma\sigma'} = 0.088$, and the initial drop radius to $R_i = 475\ lu$. The structured roughness size and height are set to 4 *lu* and 5 *lu* (instead of 4 *lu* which is consistent with the method for applying the adhesion forces in this model), respectively. This was to simulate 10 *µm* square pillars used in the experimental work of (Kwon et al., 2011). The droplet size selected from the same work was 7*μl*, which leads to droplet radius size of 1186.7*μm*. The selection of the model parameters ensured a geometrical similitude with ratio 2.5 *μ/lu*. A droplet was placed in the middle of a symmetrical domain, and the interfacial tension was calculated as $\gamma_{LV} = 0.035\ mu/ts^2$ using Laplace's pressure equation. A gravitational acceleration source term $g = 1.96\times10^{-9}\ lu/ts^2$ was used. The imposed source term resulted in a Bond number $B_o = 4\Delta\rho g R^2/\gamma_{LV} = 0.0758$, consistent with the case from experimental reference (Kwon et al., 2011). The simulations were carried out by placing the droplets on the various structured surfaces and were stopped after reaching a steady state contact angle. The vapor fluid-solid interaction constant was set to $G_{ads}^{B} = 0.012$, while a constant $G_{ads}^{R} = -0.01$ was used for the liquid to tune the surface chemistry of the smooth wall. In the SC model it is customary to use a value for the solid-fluid interaction, which is an order of magnitude smaller than the fluid-fluid constant $G_{\sigma\sigma'}$. These conditions led to 110 *degrees* static contact angle on smooth surfaces. The bounce back condition was implemented at the domain lower boundary with the structured base surface and periodic boundary at the left and right surfaces. Free boundary was applied at the top surface. 2D simulations were used in this section due to the geometrical constraints that are imposed in order to simulate the real physical case from reference (Kwon et al., 2011).

For the domain and conditions mentioned above, the simulations, which results are presented in Fig. 5 show that the pivotal spacing is 16 *lu*, which is similar to spacing 40*μm* from reference (Kwon et al., 2011). Under this condition the energy state for 7*μl* droplet is Cassie (Kwon et al., 2011), and the SC model produces the right value of apparent contact angle as calculated by the Cassie theory without any correction.

It is also observed that correction is not needed for spacing ranging between 16 and 18*lu*. The reason behind this lies in the fact that a balance occurs between larger spacing induced model capillary pressure and the sagging effects of the droplet due to the pressure difference across the interface.

Between spacing > 18 *lu* and < 40 *lu*, the droplet should not exhibit Wenzel state as the physical cases of reference (Kwon et al., 2011) indicates. The simulation results show that the model does not produce droplets which follow strictly the Cassie behavior. The droplet stable states in this range reveals a similarity in behavior to what was described in reference (M Nosonovsky & Bhushan) as 1D scenario of wetting transition. The 1D wetting transition is characterized by the presence of liquid only in the depressions closer to the three-phase contact line. This seems to be reasonable considering that transitional phase between Cassie and Wenzel states is expected to happen when increasing the roughness spacing for the same droplet size. The achieved apparent contact angles for the droplets simulations in this range of spacing are closer to these calculated by the Cassie equation. Furthermore the observation of spacing 20*lu* wetting behavior, indicates that the transition does not start at the contact line as suggested in the de-pining of the contact line hypothesis, nor via the nucleation mechanism which hypothesizes that the transition starts at the drop center (M Nosonovsky & Bhushan).

Transition is observed to start at an asperity closer to the contact line and propagate towards the contact line when the spacing increases. This can be explained by the fact that a higher pressure difference across the interface of large droplets (larger droplets have lower pressure difference) is required to drain the suspending fluid from the cavities closer to the center; hence sagging is not feasible around the droplet center for spacing ranging from 22 to 40 *lu*.

Spacing 20 *lu* represents a special case, where wetting occurs only one spacing before the contact line and does not propagate towards the contact line. A possible reason for the non-wetting behavior in the depression before the contact line is that the droplet interface might have had support from the compressive component of the flow during drainage. This additional pressure component could have helped the capillary pressure induced by this particular spacing to overcome the droplet Laplace pressure in the last cavity before the contact line and maintain some vapor in the cavity.

Table 4.1 Detailed parameters and results of simulations are shown in the table here. Cos (θ_e) on the flat surface for the present simulation is -0.342.

No.	a	B	b/a	H	A	Cos($\theta_{c/w}$)	($\theta_{c/w}$)	ξ_{R475}	θ_s	% Error
Surf. (1)	4	8	2	5	0.111	-0.927	157.955	-0.550	153.500	2.821
Surf. (2)	4	12	3	5	0.063	-0.959	163.511	-0.910	163.000	0.313
Surf. (3)	4	16	4	5	0.040	-0.974	166.826	-1.000	164.000	1.694
Surf. (4)	4	20	5	5	0.028	-0.982	169.029	-1.000	169.000	0.017
Surf. (5)	4	24	5.5	5	0.024	-0.987	170.600	-1.000	164.000	3.869
Surf. (6)	4	30	6	5	0.020	-0.991	172.262	-1.000	168.000	2.474
Surf. (7)	4	40	10	5	0.008	-0.354	110.864	-1.035	119.000	-7.339
Surf. (8)	4	60	15	5	0.004	-0.349	110.408	-1.027	118.000	-6.876

For spacing ≥ 40 *lu* correction is required to produce Wenzel condition as this is in conformance with the experimental results presented by (Kwon et al., 2011). Without correction and beyond spacing 40 *lu*, the simulated droplets are observed to sag in a remarkable manner due to a deficit in the capillary pressure in comparison to the Laplace pressure. This is caused by the large distance between the nearby peaks which reduces the support of the interface. The uncorrected apparent contact angle for spacing > 40 *lu* shows about 45% error compared to the calculated angle by the Wenzel equation.

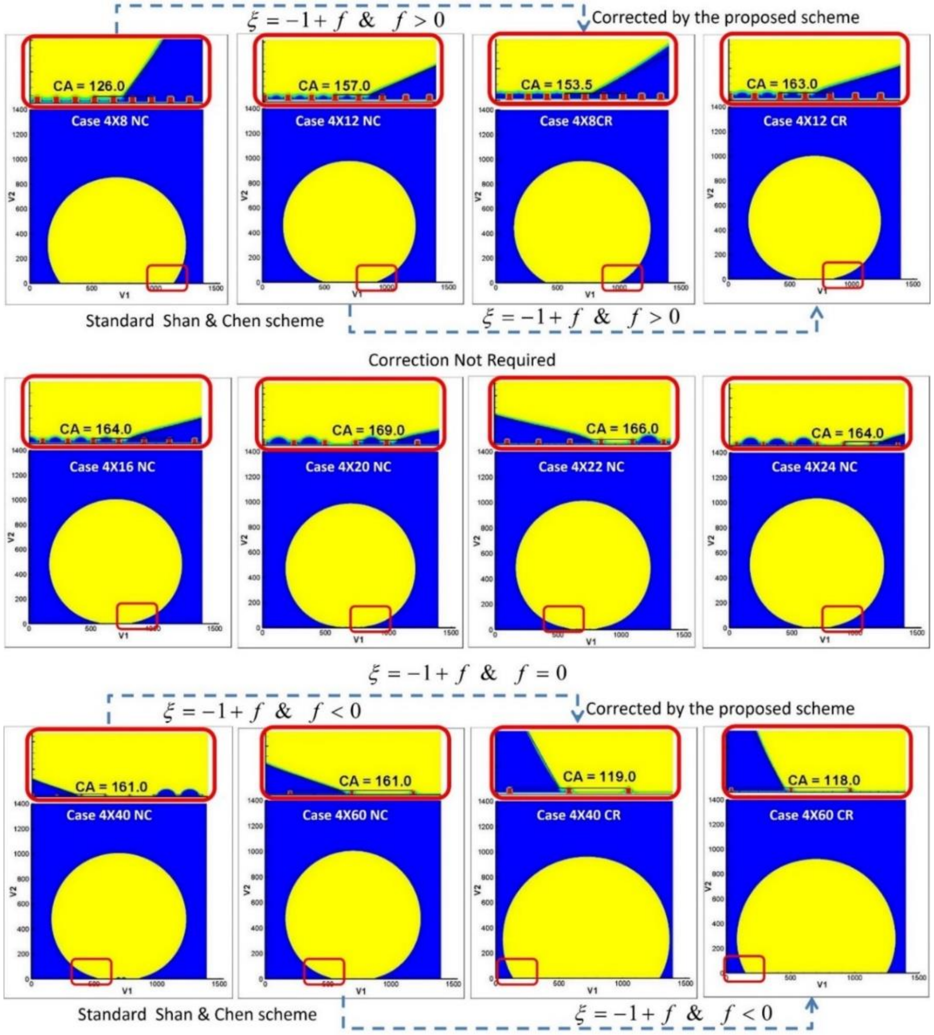

Fig. 4.5. Phase field contours for droplets resting on surfaces with different spacing. The middle section depicts the pivotal case and others where no correction is required and the angle matches Cassie's calculated apparent angle. The upper set presents the below pivotal spacing cases where a correction with *f* > 0 was made. The lower set shows the above pivotal spacing cases where a correction with *f* < 0 was made in order to match the apparent angles with the calculated theoretical values.

In table 1, ‘a’ is the roughness’ width, ‘b’ is the roughness’ spacing, ‘H’ is the roughness height and ‘A’ is the ratio from Eq. (4.7). The angles θ_e , $\theta_{c/w}$ and θ_s are the static, apparent and simulation angles, respectively. All apparent angles but the last two are calculated by the Cassie equation. The last two are calculated by Wenzel’s equation. The results are consistent with the behavior of the droplets shown in (Kwon et al., 2011).

4.5 Robustness of the proposed method

The proposed model was tested for robustness by using the two extreme cases of surface (1) and surface (8) from table 1. The simulations’ domains were characterized by a structure height of 3 *lu* which is the minimum acceptable height, due to the diffuse nature of the droplet interface and another roughness height of 10 *lu*.

For static angle above critical and based on the Cassie theory a non-wetting droplet apparent angle should not be affected by the roughness height, meanwhile for a wetting droplet the Wenzel theory predicts an increase in the apparent contact angle with the increase of the roughness height.

The results of surface (1) for structure height of 3 *lu* are presented in Fig. 4.6 show slight deviation from the achieved angle with height 5 *lu*. However the simulation results for the structure with height 10 *lu* produced the same results as the baseline simulation. This results is in compliance with the Cassie theory.

The results of surface (8) for a structure height of 3 *lu* showed deviation from the simulation of the same surface with structure height 5 *lu*. The simulation produced an apparent angle with -2.8 percent difference from the calculated angle by the Wenzel theory, which is an improvement over the baseline simulation.

Surface (8) with height 10 *lu*, exhibited compliance with the Wenzel theory principle; however a much larger apparent angle was achieved from the simulation.

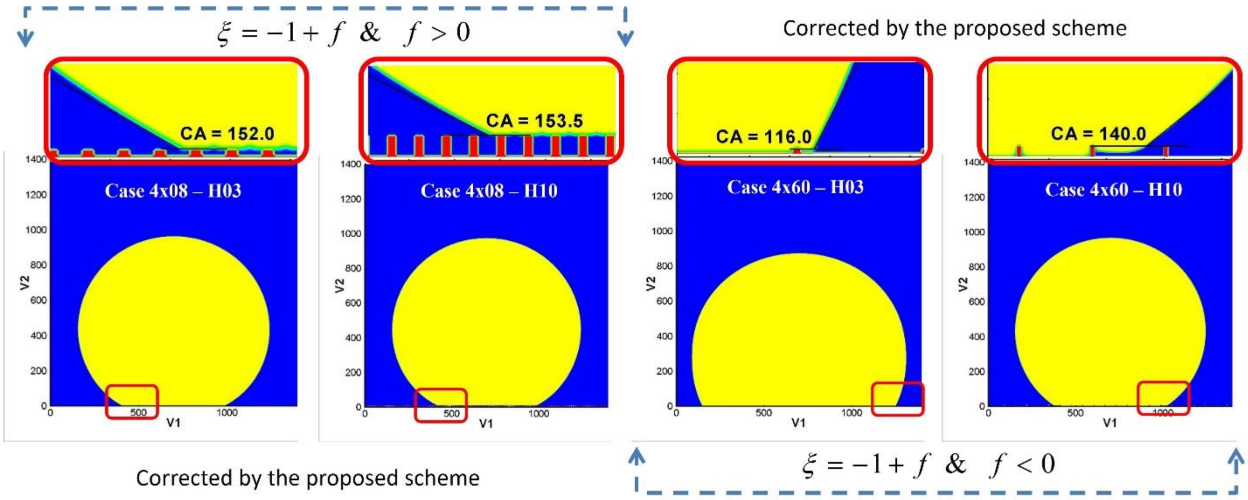

Fig. 4.6. Phase field contours of droplets placed on surface 1 and surface 8 from table 1. Two roughness heights were used to test the robustness of the model. The phase field contours show good adherence to the Cassie state and good compliance with the Wenzel theory for the lower height. The model does not comply with the Wenzel state for high height

For a static angle of 110 *degrees* and structure spacing of 60 *lu*, the Wenzel theory predict a decimal change in the apparent angle for a change in the structure height. Under the prescribed condition, the model does not comply with the Wenzel theory, since it overestimates the apparent contact angle.

4.6 Notes on the Dynamic angle in the standard Shan and Chen Model

In attempting to simulate the dynamic behavior of droplets on surfaces with structured roughness, the standard SC model was only capable of mimicking the non-reversible transition from Cassie to Wenzel state when the droplet was forced against the structured surface. Droplet evaporation and dropping droplet from height simulations were not feasible to replicate with the standard SC model.

The squeezing of a droplet towards the rough surface is shown in Fig. 4.7, where a source term was applied on top of the droplet interfacial nodes. Those nodes were identified by a phase field $\rho^N = \left(\rho^\sigma - \rho^{\sigma'}\right) / \left(\rho^\sigma + \rho^{\sigma'}\right)$, with normal vector horizontal components ranging from $0 < -\partial_x \rho^N / \left|\nabla \rho^N\right| < 0.1$. A source term, mimicking the movement of a pipette pushing the top of the droplet, was imposed for a short period of time after which, the droplet was left to recover.

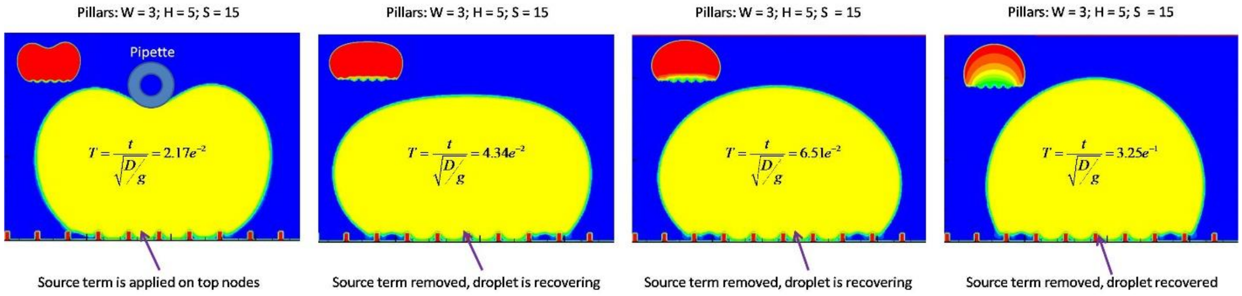

Fig. 4.7. Phase field contours of a squeezed droplet in 181x121 *lattice units* domain. The source term was removed at dimensionless time 0.02176 and the droplet was left to recover. The simulation domain and conditions are similar to those shown in Fig. 4.3 for roughness spacing of 15 *lattice units*.

After stabilization it was observed that despite the impalement of most of the surface, some vapor was trapped between the droplet and the very end of the structure; however the droplet in Fig. 4.7 showed a Wenzel state characterized by a small contact angle. The trapped vapor could be due to the fact that the source term was applied at small number of nodes on the droplet top interface to simulate the effect of using small size pipette. Further investigation and improvement of the dynamic behavior of the standard SC model may be the subject of future work.

CHAPTER 5

LATTICE BOLTZMANN SIMULATIONS FOR DISTURBED PARABOLIC FLOWS WITH SINGLE DROPLET ON SMOOTH PLANES

The Lattice Boltzmann method is used to analyze the sliding and rolling of droplets on flat horizontal surfaces. This work identifies a critical channel Reynolds number for a given droplet Weber number beyond which, the fluid transport phenomenon becomes ineffective and it comes at the account of higher energy cost for low benefits.

It is important to note that the contact angle hysteresis (CAH) is an important parameter in understanding drop motion (the rolling-off or sliding-down behavior) on a surface. On non-ideal surfaces, microscopic defects such as morphological as well as chemical are usually present. The varying contact angle formed between the flowing liquid and the solid surface, reflects the balance between the capillary and the viscous forces. The CA depends on whether the liquid is advancing over the surface or receding, resulting in CAH, which is the difference between the advancing and receding contact angles ($\Delta\theta = \theta_{adv} - \theta_{rec}$).

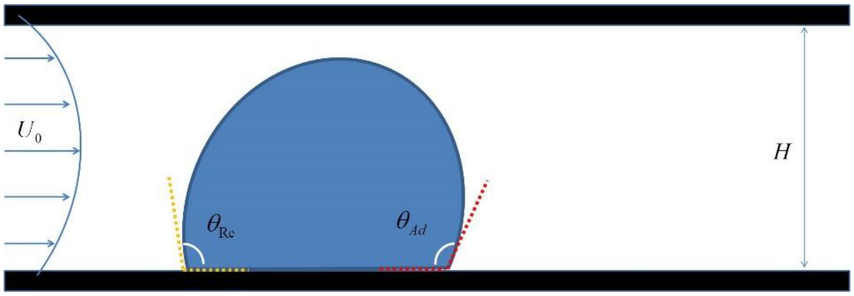

Fig 5.1: Description of a moving droplet on a micro-channel lower surface with an indication of the flow characteristics and the two associated contact angles.

For surfaces with roughness carefully controlled and patterned, the CAH could be as low as < 1° (Gupta, Ulman, Fanfan, Korniakov, & Loos, 2005) where the liquid travels easily along the surface. A large value in hysteresis indicates that the system is not at equilibrium. On superhydrophobic coating with which a droplet of water can roll on the surface, increasing the static CA up to ~ 180° will result in a reduction of the CAH due to the decreased contact with the solid surface caused by the air pockets beneath the droplet(Bhushan & Jung, 2011).

It is evident from the results of multiple experimental and numerical studies that superhydrophobic surfaces help make the transportation of the suspended phase more efficient in microchannels. This is true, especially when the droplets are in direct contact with the surfaces of the constraining geometry. However, in microchannels the effect of the compressive element of the flow, which is Reynolds number dependent, in relation to the Weber number, which determines the droplet deformability, is not investigated. The intricate relationship between these two dimensionless numbers could help and as well deteriorate the fluid transportation in microchannels flows. The present work explores several disturbed parabolic multiphase flows between parallel plates with and without surface roughness. A critical channel Reynolds number for a preset droplet Weber number is identified as best condition, characterized with high energy efficiency for transporting the disbursed phase in microchannels.

5.1 SIMULATION RESULTS AND DISCUSSION

The following notations were used in this study: ts for lattice time step, mu for lattice mass unit and lu for the lattice spatial unit. A density ratio of $\frac{\rho_R}{\rho_B} = 16$ was used, where suffices ***R*** and ***B*** indicate the suspending and suspended fluids, respectively. A relaxation time $\tau = 0.945$ was used leading to a kinematic viscosity $\nu = 0.148 \ lu^2/ts$. The interfacial tension constant was set to $G_{\sigma\sigma'} = 0.088$ resulting in an interfacial tension of $\gamma_{LV} = 0.035$. A second order accuracy bounce back condition was used on all walls. Periodic boundary condition was used on the inlet and outlet of the domain to simulated infinitely long channel. 3D domain consisting of $95 \times 95 \times 245\ lu^3$ was used for the study of the droplet motion in microchannels with flat perfectly smooth surfaces. The gravitational constant $g = 2.18 \times 10^{-6}$ was used to maintain a Bond number $B = 4\Delta\rho g R^2 / \gamma_{LV} = 0.758$.

Multiple source terms F were used, from which their respective average velocities were derived as follows:

$$\bar{U} = \frac{2}{3}\frac{h^2 F}{2\rho\nu} \tag{5.1}$$

The channel Reynolds number was calculated as:

$$\mathrm{Re}_{ch} = \frac{\bar{U}H}{\nu} \tag{5.2}$$

where H was the channel height, $h = \frac{H}{2}$ and $\bar{U}$ was the flow average velocity. The droplet Reynolds number was calculated by:

$$\mathrm{Re}_{d} = \frac{\bar{U}d}{\nu} \tag{5.3}$$

Several Weber numbers We resulted from the various simulations and they were calculated by the following equation:

$$We = \frac{2\rho\bar{U}^2 R}{\gamma} \tag{5.4}$$

A dimensionless approach was used for the analysis of the results. The channel height H was selected as a characteristic length, $U_0 = \frac{3}{2}\bar{U}$ the undisturbed centerline flow velocity, as characteristic velocity, and the inverse shearing strain rate $\dot{\gamma}^{-1} = \frac{H}{2U_0}$ as characteristic time.

To analyze the results in dimensionless manner the power required for moving the fluid in the channel is calculated as follow:

$$q = \int_{-h}^{h}\int_{-h}^{h} u\,dx\,dz = -\left(\frac{2}{3}\right)^2 \frac{h^4}{\mu}\left(\frac{\partial p}{\partial y}\right) = 0.444\frac{h^4 \Delta p}{\mu \ell} \tag{5.5}$$

where q is the volumetric flow rate through the channel and $F = {}^{\Delta p}\!/_{\ell}$.

The power required for moving the undisturbed flow through the channel is calculated by:

$$\mathrm{P} = q\,\Delta p = 0.444\frac{h^4 F^2 \ell}{\mu} \tag{5.6}$$

Since the transport of the suspended phase is the focus of this work's interest, the droplet mass center is tracked and the velocity is calculated by differentiating the mass center displacement using second order accuracy finite difference scheme. A droplet power number is introduced as follows:

$$\mathrm{P}_d = \frac{\rho_d \cancel{V}_d V_{dmc}^3}{\ell} \tag{5.7}$$

where ρ_d is the droplet density, $\cancel{V}_d$ is the initial droplet volume, V_{dmc} is the droplet mass center terminal velocity and ℓ is the domain length.

5.2 Effects of the droplet radius on multiphase fluid transportation in 3D flat perfectly smooth microchannels

The 3D domain described in this section was used for determining the effects of the dimensionless radius on the movement of one droplet sliding on ideal smooth surface in a micro-channel. The droplet radii were normalized by half of the channel height. A source term $F = 2.5\times10^{-6}$ was used, yielding an average undisturbed velocity $\bar{U} = 0.0124$ and channel Reynolds $\mathrm{Re}_{ch} = 7.98$. The adhesion constants $G_{ads}^{B} = 0.011$ and $G_{ads}^{R} = -0.0095$ were used for the two phase fluid to warrant a static contact angle of 105^{o}.

Four droplets *R* = 5 -30 were used to cover a dimensionless radii range of R_{dS} = 0.1- 0.63. Fig 5.2 shows the various droplets phase field contours, a section in the yz plane for their horizontal and vertical velocity contours. It is obvious from Fig. 5.2-D that a droplet with larger dimensionless diameter moves in the domain at higher terminal velocity; however this comes at much higher power price. The power growth ratio for the case with droplet radius *R* = 30 *lu* to the power required to move the small droplet with radius *R* = 5 *lu* is $R_{P\_Gth} = 1589$. The droplet velocity gain ratio is $R_{V\_Gn} = 1.95$, which is very humble when compared to the required power growth.

This behavior is caused by the parabolic nature of the flow, in which large droplet size allows more energy from the flow to be dissipated into it. This results in a higher droplet terminal velocity. Furthermore, the larger the dimensionless radius, the greater the droplet's Weber number is. This causes more energy to be spent into deforming of the droplet, hence the higher power cost.

A combination of the two factors, i.e. higher momentum in the central region of the channel and higher Weber number lead to the fast transportation of the larger droplet, but at very high power cost from the suspending fluid. A power curve fit was used to describe the relationship between the dimensionless powers as a function of the dimensionless radius.

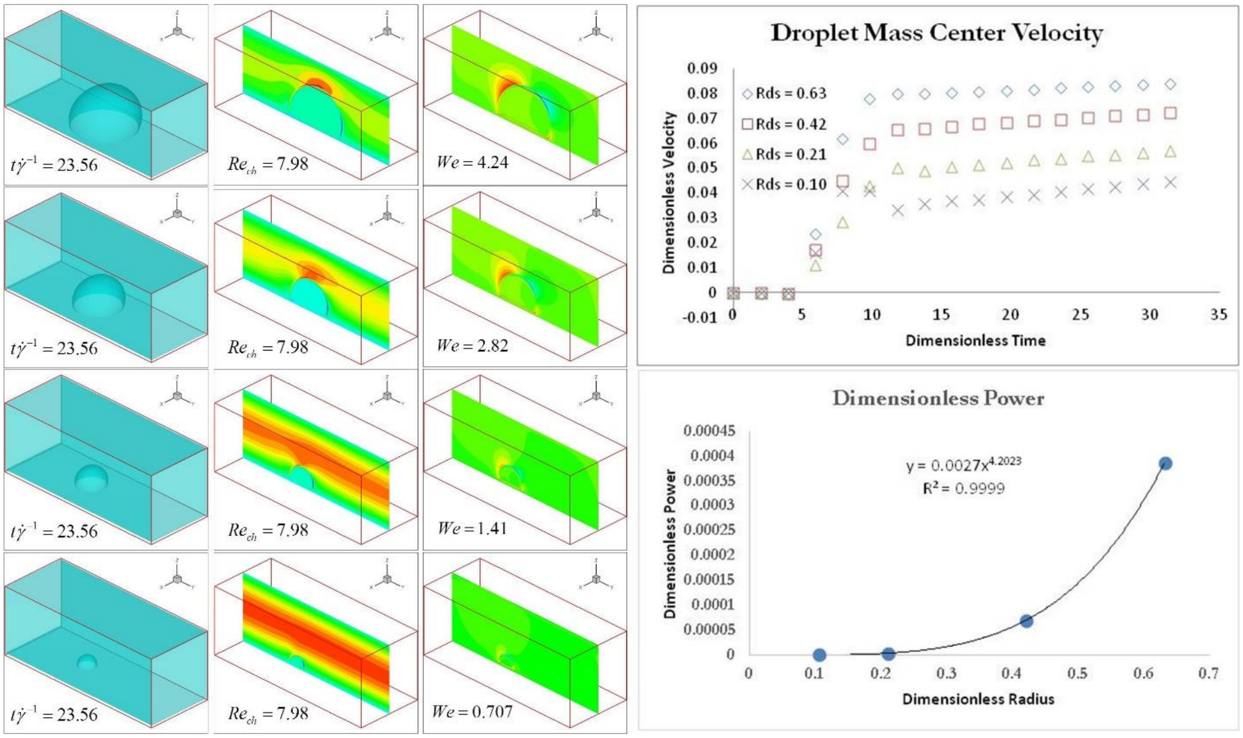

Fig 5.2: **A-** Phase field contours for droplets moving on flat smooth surfaces. **B-** Horizontal velocity contours slide in the yz plane. **C-** Vertical velocity contours. **D-** Droplet mass center horizontal velocity and curve fit for the dimensionless power required to move a single droplet in the domain with the radius normalized by half of the channel height.

From Fig. 5.2-D it is clear that a single droplet requires very minimal power compared to moving the suspending flow itself. The power required to move one single droplet could increase slightly if the interface pinning due to the surface imperfection is taken into consideration.

5.3 Effects of the Weber number on multiphase fluid transportation in 3D flat perfectly smooth microchannels

The effects of the Weber number on the transport of the suspended phase, was investigated through the movement of three droplets with their radii fixed at *R* = 20 *lu.* The interfacial tension constant was varied in between $0.75 \leq G_{\sigma\sigma'} \leq 1.0$, thus yielding a Weber number range of $2.49 \leq We \leq 3.32$. Wider range was not feasible to implement since the SC model becomes unstable with regards to conserving the mass of the suspended phase and the interface thickness is directly related to the interfacial tension constant. However if water is used as a basic liquid, Glycerol and many aqueous solutions such as Acetic acids plus water and ethanol plus water can be covered with the described range. One single source term $F = 2.5 \times 10^{-6}$ was used in the simulations to maintain the same Reynolds number. Static simulations of the three conditions were executed to investigate the influence of the interfacial tension change on the static contact angles. The deviation from the initial value of 105^{o} was less than 2 %.

As it is shown in Fig. 5.3-D a moderate change of the Weber number, has a transient effects on the droplet with the least interfacial tension velocity, which start at higher dimensionless velocity but it eventually decays to levels close to those of the rest of the droplets. This can be explained by the fact that with higher Weber number the droplet is able to deform and get below the flow channel center, which leads to a drop in its velocity. It is interesting to notice from Fig. 5.3-C, that a droplet mass center higher velocity is always associated with high suspending flow positive z component velocity at the rear top of the droplet and low negative velocity at the front top. Fig. 5.3-B shows that the droplet with the highest mass center velocity has the highest suspended flow y component. This is indicative of the level of disturbance that the droplets impose on the suspending flow and thus the level of energy dissipated into the movement of the transported droplets.

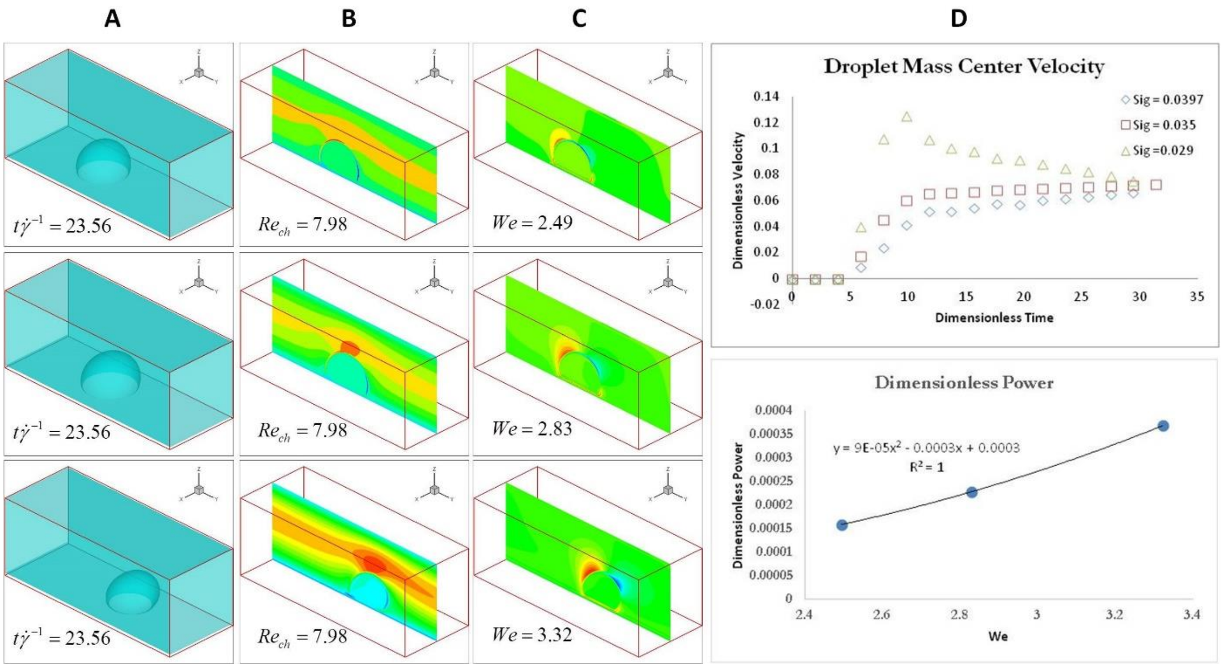

Fig 5.3: **A-** Phase field contours for droplets moving on flat smooth surfaces with different interfacial tensions. **B-** Horizontal velocity contours slide in the yz plane. **C-** Vertical velocity contours. **D-** Droplet mass center horizontal velocity and curve fit for the dimensionless power required to move a single droplet in the domain with the radius normalized by half of the channel height.

The power growth ratio for the case with droplet Weber number $We = 3.32$ to the power required to move the same size droplet with Weber number $We = 2.49$ is $R_{P\_Gth} = 1.33$. The droplet velocity gain ratio is $R_{V\_Gn} = 1.32$, which is comparable to the required power growth.

5.4 Effects of the channel Reynolds number on multiphase fluid transportation in 3D flat perfectly smooth microchannel

To evaluate the effects of the channel's Reynolds number on the transport of the suspended phase, the droplet radius was fixed at *R* = 20 *lu* and the source term range

$F=2.5\times10^{-6}-9.5\times10^{-5}$ was used, leading to $\mathrm{Re}_{ch}=0.79-30.33$. The static contact angle was the same as in the previous simulations. Since the source terms from the various simulations were different, an average central velocity of the undisturbed flow was used in the calculation of the dimensionless time. This was done to ease the visualization and analysis of the droplet dimensionless displacement and velocity presented in Fig. 3 D.

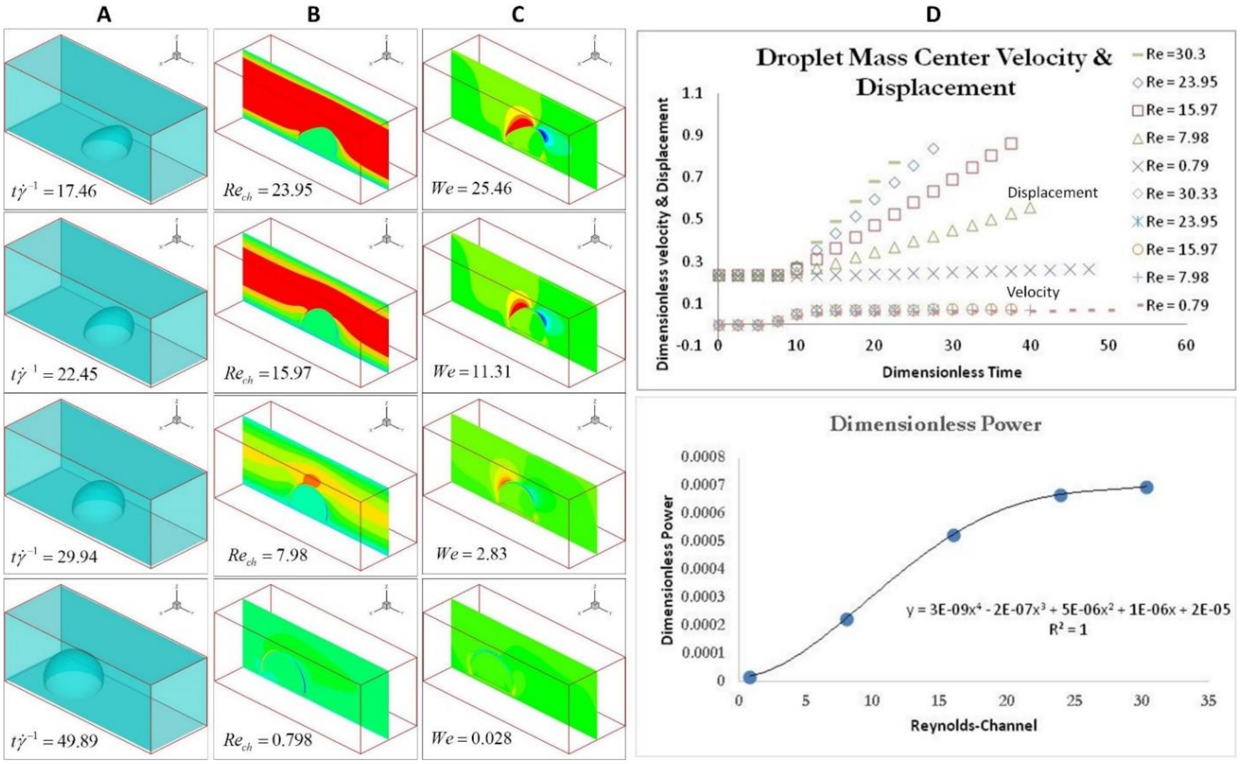

Fig 5.4: A- Phase field contours for droplets moving on flat smooth surfaces with few Reynolds numbers. **B-** Horizontal velocity. **C-** Vertical velocity contours. **D-** Droplet mass center horizontal displacement, velocity and curve fit for the dimensionless power required to move a single droplet in the domain.

With increasing channel Reynolds number, the dimensionless power number seems to peak at a certain value for a given droplet radius, and levels up after the peak as shown in the graph of Fig. 5.3-D.

The behavior of the droplet in the rising section before the peak is due to the parabolic nature of the flow and the energy spent into deforming the droplet; however after the peak it seems like the droplet deforms enough as its Weber number grows bigger, that it manages to align itself further with the flow and while it disturbs the flow relatively less it is able to maintain a large momentum. The graph in Fig. 3D for the various droplets' displacements normalized by the channel length, indicates that the displacement of the droplet with the higher channel Reynolds number is the greatest. The droplets' velocities normalized each by its undisturbed central velocity converge to about 0.07 which is related to the use of an average velocity of all cases as a reference velocity.

The power growth ratio for the case with droplet Reynolds number $Re_{ch} = 23.9$ to the power required to move the same size droplet with Weber number $Re_{ch} = 0.798$ is $R_{P\_Gth} = 32.78$. The droplet velocity gain ratio is $R_{V\_Gn} = 36.16$, which is comparable to the required power growth.

5.5 Effects of the static contact angle on multiphase fluid transportation in 3D flat perfectly smooth microchannel

Four sets of adhesion constants were used to produce four droplet static contact angles. The droplets had the same radii *R* = 20 *lu* and the source term was maintained at $F = 2.5 \times 10^{-6}$. The various droplets static angles ranged from 73 to 118 *degrees*. The aim was to investigate the effects of changing the static contact angle on the behavior of the droplets.

Fig 5.5-D show that the droplet with the highest static contact angle moves at higher speed and requires moderately higher power from the flow. It is also noticeable that static contact angles below critical exhibit smaller change in droplet speed, contrary to the behavior shown by static contact angles greater than critical. Fig 5.5-B and C show that the suspending flow is disturbed more by the droplet with the lowest contact angle. This is due to the resistance to movement that the droplets with low contact angle exercise;

however it is observed that with lower the static contact, the height of the droplet decreases. This results in lower mass center velocity, since the flow velocity and hence the flow momentum diminishes gradually below the channel centerline. This behavior is characteristic to parabolic flows.

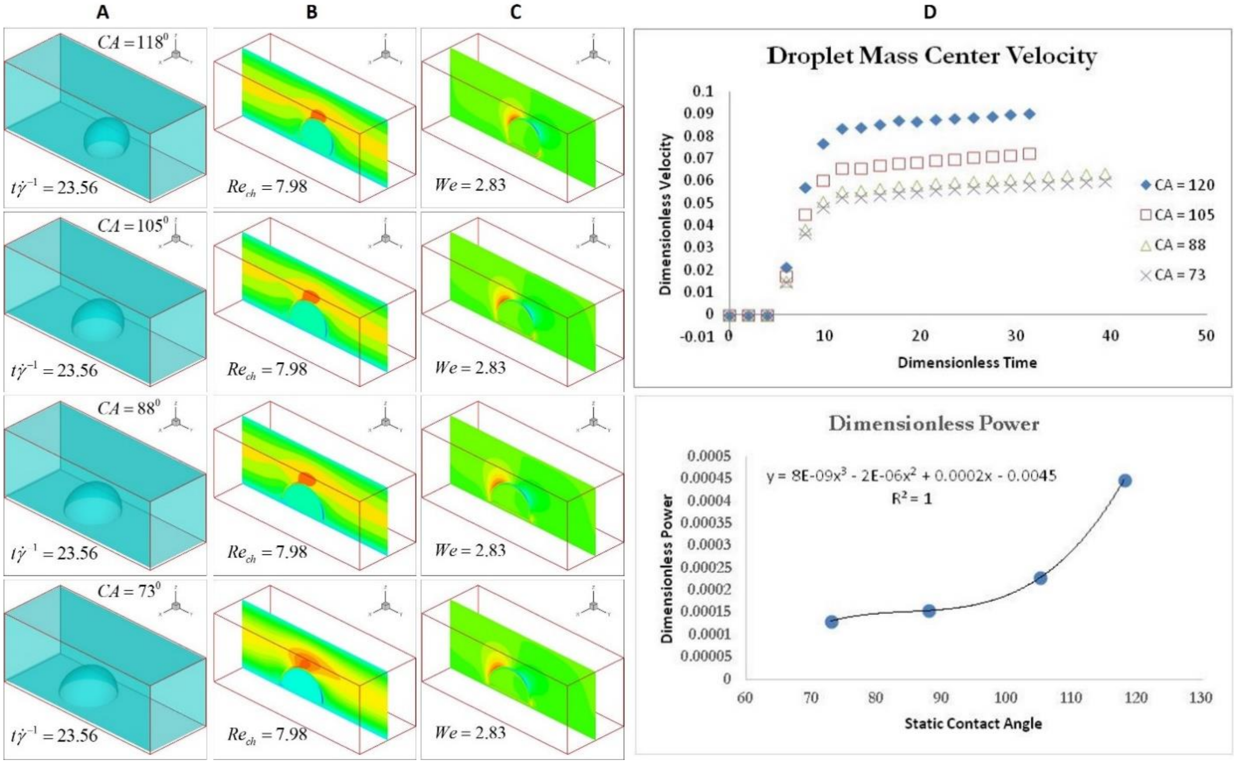

Fig 5.5: A- Phase field contours for droplets moving on flat smooth surfaces with different static contact angles. **B-** Horizontal velocity. **C-** Vertical velocity contours. **D-** Droplet mass center horizontal displacement and velocity, and curve fit for the dimensionless power required to move a single droplet in the domain.

The power growth ratio for the case with droplet static contact angle $CA = 118$ to the power required to move the same size droplet with static contact angle $CA = 77$ is $R_{P\_Gth} = 3.41$. The droplet velocity gain ratio is $R_{V\_Gn} = 1.50$, which almost twice the required power growth is.

In summary, the effects of the various factors which influence the multiphase flow transportation such as dimensionless droplet radius, Weber number, Reynolds number and static contact angle, should be taken into consideration when designing a multiphase flow transportation in a microchannel. The following guidelines are to help optimizing the design characteristics of multiphase fluid transportation:

1. The suspended phase should absorb the highest possible energy from the flow, since most of the energy is required for moving the suspending flow. This is achieved usually by larger droplets, droplets with higher Weber numbers and droplets with high contact angles.

2. Flow with optimal flow Reynolds numbers are preferable, although the droplet velocity increased drastically ($R_{V\_Gn} = 36.16$) with the increase in Reynolds number; however the suspended flow power increased by 1440 times. Higher Reynolds number could also cause evaporation of the suspended phase, which is not desirable from energy and practical perspectives.

3. Surfaces with chemistry and structure, which ensure phobic static contact angle are favorable.

CHAPTER 6

LATTICE BOLTZMANN METHOD FOR SINGLE SLIDING DROPLETS ON SLOPED FLAT AND ROUGH SURFACES

The sliding of droplets on sloped surfaces with and without roughness is numerically investigated. The Shan and Chen (SC) Lattice Boltzmann model (LBM) is used to analyze the effect of pinning on the movement of droplets placed on sloped surfaces. The model is checked for conformance with the Furmidge equation which applies to tilted unstructured surfaces. It is shown that a droplet sliding on a perfectly smooth surface requires very minimal slope angle and that pinning due to the inhomogeneous nature of manufactured smooth surfaces is the key factor in determining the minimal slope angle. The model is also used on sloped rough surfaces to check the effects of roughness on the movement of single droplets. The numerical outcomes are compared with published experimental results for validation and a dimensionless number is suggested for quantifying the degree of pinning needed to control the behavior of sliding droplets on sloped surfaces.

The present chapter confirms the adherence of the SC model to the Furmidge equation when simulating droplets moving on sloped unstructured surfaces due to gravity in three dimensional (3D) domains. The role of pinning due to imperfections in real surfaces is shown to have an important role in determining their sliding angle. The model is validated by comparison with experimental works and used for investigating the movement of droplets on sloped rough surfaces.

Surface chemistry and topography determine how a droplet of liquid sits and moves on a surface (Neinhuis & Barthlott, 1997; Onda, Shibuichi, Satoh, & Tsujii, 1996).

The contact angle is also an indication for surface hydrophobicity. A flat and smooth hydrophobic surface exhibiting an equilibrium contact angle of 110° can be converted into a superhydrophobic surface with an apparent contact angle greater than 150° by simply roughening it and without any alteration to its surface chemistry (McHale, Shirtcliffe, & Newton, 2004). Another element that plays an important role in describing the surface wetting, is the contact angle hysteresis (CAH) which helps determining the surface level of hydrophobicity (Chen et al., 1999; Youngblood & McCarthy, 1999). If a droplet is placed on a tilted surface, it will start to move when the lower droplet angle reaches the advancing angle (θ_{adv}) and the upper one reaches the receding angle of (θ_{rec}) as shown in Fig. 6.1.

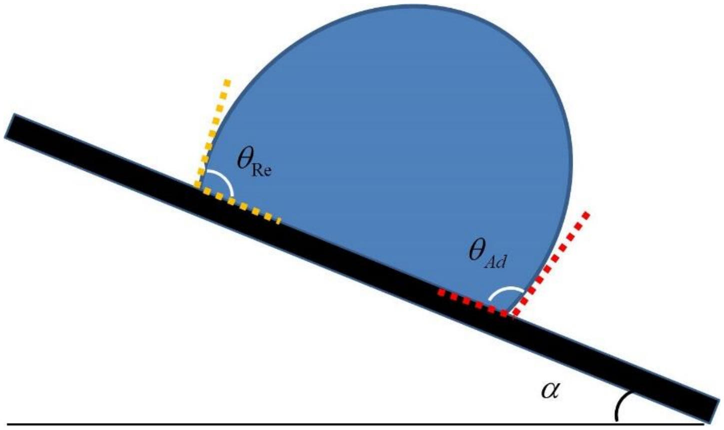

Fig 6.1: Description of a moving droplet on a smooth sloped surface showing the advancing and receding contact angles.

The downward component of drop volume (*mg sinα*) can be equilibrated if the receding angle is smaller than the advancing angle which is expressed by the Furmidge equation (Furmidge, 1962):

$$mg \sin\alpha = w\,\gamma_{LA}(cos\theta_{\mathrm{Re}} - cos\theta_{Ad}) \qquad (6.1)$$

where w is the drop width in the direction perpendicular to the plane of movement and γ_{LA} is the liquid-vapor interfacial tension.

6.1 SIMULATION RESULTS AND DISCUSSION

A 3D domain consisting of $111 \times 181 \times 111\ lu^3$ (*lu* for lattice unit) was used in the 3D simulations. The relaxation time was set to $\tau = 0.945$, resulting in a kinematic viscosity $\nu = 0.148\ \ lu^2/ts$ (*ts* for time step). The density of the suspending fluid was $\rho_B = 1\ \ mu/lu^3$, while $\rho_R = 16\ \ mu/lu^3$ (*mu* for lattice mass) was used for the suspended fluid density. The fluid-fluid interaction constant was set to $G_{\sigma\sigma'} = 0.088$ resulting in an interfacial tension of $\gamma_{LV} = 0.035$. The main case used in the simulations had an initial drop radius was $R_i = 45\ lu$. A droplet was placed in the first quarter of the domain and the simulation was stopped after *30000 ts* from the initiation of the droplet movement due to gravity. The suspending fluid-solid interaction constant was $G_{ads}^{B} = 0.011$ and a constant $G_{ads}^{R} = -0.0095$ was used for the suspended fluid for producing 105^0 static smooth surface contact angle. A gravitational constant $g = 2.18 \times 10^{-7}$ was used to produce a Bond number $B = 4\Delta\rho g R^2 / \gamma_{LV} = 0.758$. This is to simulate a water droplet with radius 1186.68 *µm* (7 *µl*) and gravity 9.81 *m/s*^{2}. No slip boundary condition was enforced on the sloped surface, periodic condition on the sides and free surface on the top surface.

A 2D domain made of 2400×1300 *lu*^{2} was used to study the droplet behavior on sloped rough surfaces. A density ratio of $\frac{\rho_R}{\rho_B} = 16$ was used. A relaxation time was set to produce the same kinematic viscosity $\nu = 0.148\ \ lu^2/ts$ as in the 3D case. The interfacial tension constant was set to $G_{\sigma\sigma'} = 0.088$. The pillar size and height in the rough surface simulations were selected as *4 lu* and *5 lu* respectively leading to geometric similitude of

2.5µm/lu. A droplet with initial radius *R = 475 lu*, was placed in the domain with its mass center located at coordinates *(650, 484)*. The gravitational constant was set to $g = 1.96 \times 10^{-9}$, yielding a Bond number $B = 0.758$ similar to the 3D simulation. The suspending fluid adhesion constant was $G_{ads}^{B} = 0.012$, while $G_{ads}^{R} = -0.01$ was used for the suspended fluid. The resulting static contact angle was 110^{0}. A second order accuracy bounce back condition was implemented on the sloped surface. Periodic boundary condition was used on the inlet and outlet surfaces and free surface at the top side.

6.2 Homogeneous and inhomogeneous smooth surfaces in 3D domain

The behavior of droplets, sliding on smooth sloped surfaces is investigated in this section. A single droplet was placed in the previously described 3D domain. Several slope angles were used in an incremental manner to determine the minimum angle required for the onset of the droplet movement.

The simulations of three droplets with initial radii $R_i = 15\ lu$, $R_i = 25\ lu$ and $R_i = 45\ lu$ moving on perfectly smooth surfaces, were used to study the sliding behavior of the droplets on ideal smooth surfaces. The simulation results are shown in Fig. 6.2.

(Rios, Dodiuk, Kenig, McCarthy, & Dotan, 2008), measured in an experimental setup the sliding angles of water droplets placed on several surfaces with different chemical structures. The reported sliding angles relative to the droplet sizes used in the experiment is reproduced in Fig. 6.2-C.

From the results shown in Fig. 6.2-C, it is evident that the simulation outcome of the minimum sliding angles adheres well to the Furmidge equation; however the simulations underestimate the sliding angles when compared with the experimental results. The difference is mainly due to the lack of pinning in the model, since the simulation surfaces are perfectly smooth, while real physical surfaces are usually imperfect.

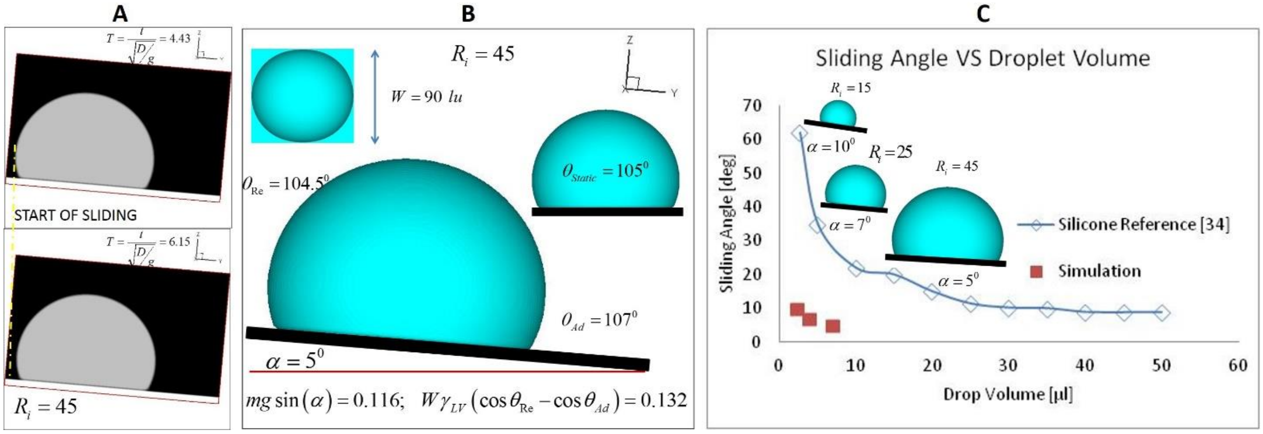

Fig 6.2: **A-** The cross section of the phase field contours for a droplet with radius *R* = 45 sliding on flat smooth surface are used at different time steps to indicate the initiation of droplet movement on 5 degrees slope. **B-** 3 D phase field contours for the droplet with the explanation of the calculation used for confirming the adherence of the model with the Furmidge equation. **C-** Sliding angles for three droplets with different radii compared with the results of reference [34].

The pinning role due to surface imperfection, which was neglected in (Rios et al., 2008), is evident from the results presented in the same reference, where PTFE with measured static contact angle of 111.9 ± 3.0 *degrees* and calculated surface energy of 31.5 *mJ/m*^{2}, required much higher sliding angles than PMMA with measured static contact angle of 72.5 ± 3.3 *degrees* and calculated surface energy of 44.1 *mJ/m*^{2}.

Table 6.1 Error between the left hand and the right hand sides of Eq. (6.1) for the smooth surfaces.

Ri	m.g.sinα	w.σ.(cosα$_R$-cosα$_A$)	% Error	θ$_R$	θ$_A$	α	W
45	0.11603757	0.132273857	12.27475	104.5	107	5	90
25	0.02782144	0.029432044	5.472284	105	106	7	50
15	0.00856267	0.008840298	3.140503	105	105.5	10	30

Few minute pillars with dimensions smaller than the interface thickness ($\forall = 1\ lu^3$ each), were used to invoke pinning. This approach was followed, since one lattice unit is the smallest dimension possible in the regular LBM mesh and because it was not feasible to simulate the randomness and physical sizes of the microscopic imperfections due to manufacturing of real surfaces. The minute pillars were positioned such that about 60% of their total area was closer to the receding angle section of the droplet. The following dimensionless number $f = {}^{A_{inh}}\!/_{A}$ was used to quantitatively assess the inhomogeneous area fraction effects on pinning, where A_{inh} was the total surface the small pillars and A is the droplet base area. The droplet base area was estimated by using the surface of an ellipse $A = \pi ab$ and the area of the minute pillars $A_{inh} = n \times 5\ lu^2$ with *n* indicating the number of pillars. The halves of the minor and the major axis of the droplet base a, b were measured from the simulation and the number of minute pillars n was found by trial.

The simulation results of the inhomogeneous smooth surface with $f = 1.3 \times 10^{-2}$ are shown in Fig. 6.3. The droplet with initial radius $R_i = 45\ lu$ started moving when an angle of 25 *degrees* was reached. The droplet movement, which was associated with the largest contact angle hysteresis of 11 *degrees,* occurred around $T = {}^{t}\!/_{\sqrt{2R_i/g}} = 5.17$ dimensionless time steps. The solid/liquid contact diameter in the direction perpendicular to the direction of movement was measured from the droplet phase field contours as $W = 94\ lu$. The droplet mass in the left side of Eq. (6.1) was calculated with the initial volume and density of the droplet. The left side of Eq. (6.1) yielded 0.563, while the right side equated to 0.6. With a difference of 6 *%* between the two sides of the equation, the model outcome agrees reasonably with the Furmidge equation.

For a water droplet with a volume of 0.7 *µl* placed on a silicone substrate in reference (Rios et al., 2008),, the sliding angle in the presented graph reads ~27.5° and the static contact angle was measured as 103°± 2.5°. The simulation results of 25 *degrees* slope angle and 110 *degrees* static angle, closely matched the reported results by (Rios et al., 2008).

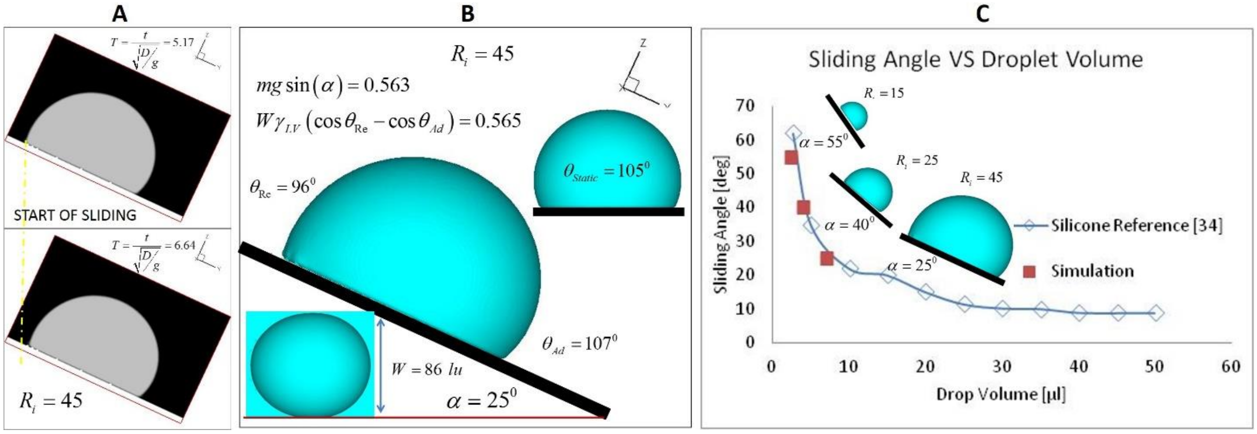

Fig 6.3: **A-** The cross section of the phase field contours for a droplet sliding on flat surface with 22 miniature pillars are used at different time steps to indicate the initiation of droplet movement on 25^o slope. **B**- 3 D phase field contours for the droplet with the explanation of the calculation used for confirming the adherence of the model with the Furmidge equation. **C-** Sliding angles for three droplets with different radii compared with the results of reference [34].

Table 6.2 Error between the left hand and the right hand sides of Eq. (6.1) for the surfaces with induced roughness.

Ri	m.g.sin(a)	w.sig.(cosr-cosa)	% Error	θ_R	θ_A	α	W	f
45	0.56266628	0.565408157	0.484938	96	107	25	86	0.014161
25	0.14674138	0.149049018	1.548239	100	105	40	44	0.014469
15	0.04039275	0.041531843	2.742706	102.5	105	55	28	0.01421

Beside the main simulation case with droplet radius $R_i = 45\ lu$, two additional simulations were executed with radii $R_i = 25\ lu$ and $R_i = 15\ lu$ respectively. The simulations of the smaller droplet maintained $f \approx 1.3 \times 10^{-2}$ dimensionless number. The results of two droplets are presented in Fig. 6.3C, where a close agreement between the simulations and experiment is shown.

3.1 Pinning on structured rough surfaces in 2D domain

The 2D domain and conditions described in the beginning of this section were used on a 25 *degrees* sloped rough surface characterized by regular structure width of 4 *lu*, spacing of 16 *lu* and height of 5 *lu*. It is known that rough hydrophobic surfaces enhance the sliding-rolling of droplets, which leads to smaller sliding surface angles (Lv, Yang, Hao, He, & Zheng, 2010), and low contact angle hysteresis; however the simulation results showed a different behavior. The behavior is similar to the experimental results discussed in (Bommer et al., 2014) for ethylene glycol with initial static contact angle of 90 *degrees*, where the droplet pinned to the rough surface and it deformed to a large extent, thus exhibiting very large hysteresis without moving.

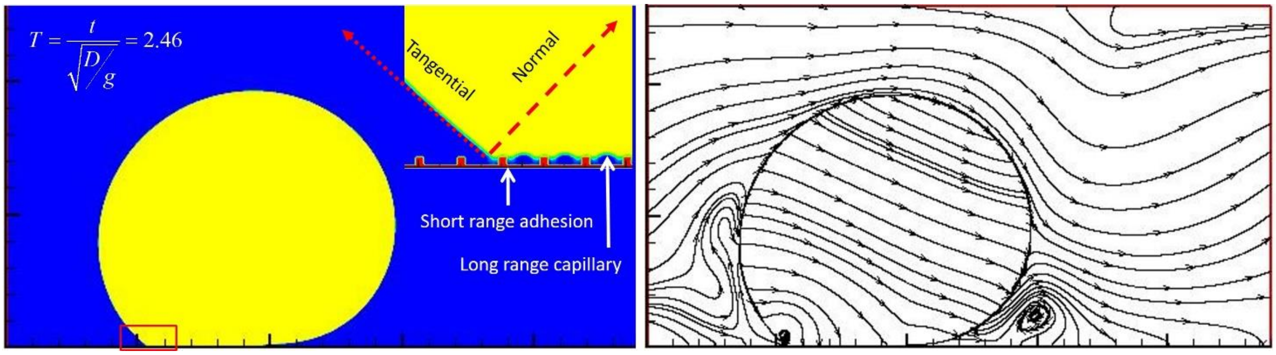

Figure 6.4: Phase field contours for droplet's pinning to a regularly structured surface with4x16 surface spacing and 25 *degrees* slope angle.

A close observation of the model results could be used for analyzing the effects of pinning on rough surfaces and it leads to the following hypothesis:

- **a-** Pinning, away from the droplet external three-phase contact line is due to the local nature of the adhesion force, which is a short range force and it is only applicable where a surface exists. Pinning is strongly observed at the corners of the asperities, where the droplet contacts the vertical and horizontal sections of the structure and the interface reshapes itself in accordance with the structure geometry. The adhesion is counteracted upon by the capillary force. This is a long range force, which magnitude is higher at the center of the spacing and it is lower in the vicinity of the surface wall. This is well explained in the discussion of the free surface boundary condition in (Colosqui, Kavousanakis, Papathanasiou, & Kevrekidis, 2013), which interface's deflection is governed by the 2D interface evolution differential equation. The interface deflection is parabolic by nature, and it can frown or smile depending on the pressure difference across the interface. The equation is given by:

  $$\Delta P = -\Im \frac{d^2\eta}{dx^2} \Bigg/ \left[1+\left(\frac{d\eta}{dx}\right)^{\frac{3}{2}}\right]^2 \qquad (6.3)$$

  where $\Im$ is the coefficient of the surface tension of the fluid and η is the interface deflection.

  It is important to state that the strength of pinning at the droplet base determines whether the droplet slides rolls or slides and rolls on the inclined surface.

- **b-** De-pinning of the receding side at the three-phase contact line seems to be the most important factor influencing the droplet movement on rough surfaces. This work suggests that this is due to the interfacial tension force at the contact line, which acts against the local adhesion force beside the effects of the component of the body force transmitted through the interface. In a physical system this force acts in a tangential direction to the interface and is expected to be more efficient in defeating the local action of the adhesion force depending on the fluid surface tension strength. This explains the reason why it is easier for a droplet of water to roll/slide on a rough surface in comparison with an alcohol droplet.

c- The advancing side of the interface does not help the droplet movement in case of pinning of the receding side, since the interface at the advancing side is prevented from touching the structure due to the lack of deformation posed by the droplet capillary number and the support of the interface by the vorticial activity shown by the streamlines of Fig. 6.5.

This model behavior, which is in contradiction with the physical behavior of a water droplet on superhydrophobic surface, is probably due to the method used for imposing the pressure jump through the interface.

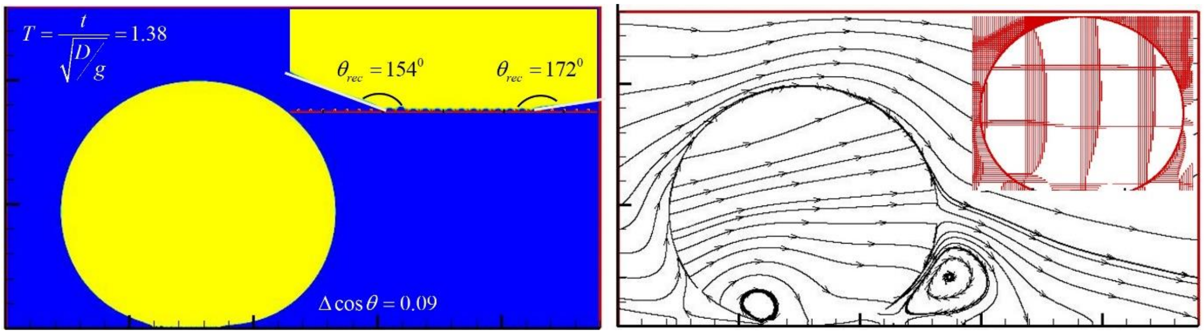

Figure 6.5: Phase field contours for droplet with de-pinned receding side of the interface on a regularly structured surface with 4x16 surface spacing and 10 *degrees* slope angle. The inset in the left part of the figure show the velocity vectors inside the droplet.

In most famous multiphase flow schemes, among them the SC, creating an interfacial tension is accomplished by applying a source term in the direction normal to the interface, meanwhile the real interfacial tension acts in a tangential direction to the interface.

Based on the above discussion and to heuristically prove that it is only required to de-pin the receding side of the interface for the droplet to move on surfaces with minimal slope angles, the adhesion force was relaxed in the model in the surrounding of the first roughness corner. This was achieved by tracking the droplet interface and locating the receding contact line nearest surface roughness.

In Fig. 6.5 it is clear that the droplet crawls as it was described in (P. Hao, Lv, Yao, & He, 2010) (slides and rolls partially) when the receding side is disengaged from the structure. As an outcome of de-pinning the droplet does not disturb the surrounding flow enough such that the vorticial activities in the area behind the advancing side cease from cushioning the interface, thus allowing the droplet to advance by adhesion to the next roughness edge on the surface.

Comparing the sliding angle and contact angle hysteresis shown in Fig. 3 of reference (P. Hao et al., 2010) with our results show a reasonable agreement for pillars size 4*μm* and spacing 14*μm*. The results of velocity vectors shown in Fig. 6.5 show a very good qualitative match with the PIV results shown in Fig. 5 of reference (P. Hao et al., 2010).

This work showed a good agreement with published theoretical and experimental results with respect to the Furmidge formula. Pinning of the receding side was shown to have a major influence on the behavior of droplets on sloped surfaces.

CHAPTER 7

CONCLUSION AND RECOMMENDATIONS

7.1 Conclusion

A pseudo potential LBM based Shan and Chen model is best suited for study of static and dynamic contact angles over flat surfaces because contact angle and interface are controlled by nonlocal interaction potentials and are not modeled, unlike in other similar mesoscopic numerical models.

However in the present work, it is shown that the Shan and Chen model does not accurately predict the Cassie and Wenzel apparent contact angles on rough surfaces. Due to the indifference of the model to the capillary length, the Shan and Chen model results in the droplet impalement into the asperities for narrower spacing and thus predicts a lower contact angle. For larger spacing, the study shows the transition of droplet from Cassie to Wenzel state associated with an increase in the roughness' spacing. The change in the droplet wettability is due to the reduction of the interface support between the asperities as the spacing increases. The resulting contact angle is however higher than the angle predicted by Wenzel's equation.

The present work introduces a correction to the capillary pressure into the Shan and Chen model based on the physical explanation provided by (Kwon et al., 2011); and performs the simulations by mimicking a water droplet of $7 \mu l$ and pillar width of $10 \mu m$. Spacing between the pillars varied from $20 \mu m$ to $150 \mu m$. The modified LBM scheme presented in this work is found to accurately predict the contact angle of droplets on structured rough surfaces.

The strength of this model is in its simplicity and its capability of reproducing the apparent contact angles of Cassie and Wenzel. This makes it a potential platform for the simulation of more complex cases involving superhydrophobic surfaces with structured surfaces.

Then, the model is used to analyze the movement of droplets in contact with flat horizontal surfaces. This part of work identifies the main factors, which influence the multiphase fluids transport in squared channels. Effects of dimensionless radius, Weber number, Reynolds number and static contact angles are evaluated by calculating the power required for moving single droplets in comparison to the power needed for moving the undisturbed flow in the channel. Guidelines for optimizing the design of such flow are presented.

In the last part of work, the sliding-rolling of droplets on sloped surfaces with and without roughness is numerically investigated. The Shan and Chen (SC) Lattice Boltzmann model (LBM) is used to analyze the effect of pinning on the movement of droplets placed on sloped surfaces. The model is checked for conformance with the Furmidge equation which applies to tilted unstructured surfaces. It is shown that a droplet sliding on a perfectly smooth surface requires very minimal slope angle and that pinning due to the inhomogeneous nature of manufactured smooth surfaces is the key factor in determining the minimal slope angle. The model is also used on sloped rough surfaces to check the effects of roughness on the movement of single droplets. The numerical outcomes are compared with published experimental results for validation and a dimensionless number is suggested for quantifying the degree of pinning needed to control the behavior of sliding droplets on sloped surfaces.

7.2 Recommendations for future work

The recommendation for future works with relation to the current work is the study of capillary driven fluid transportation phenomena. The research should focus on the following:

- Create specialized patterned structures aimed at creating targeted roughness gradient.
- Investigate Marangoni stress effects on the fluid movement due to the change in interface curvature by the roughness gradient.

Understanding this physical process should facilitate the creation of structures aimed at targeted liquid delivery

REFERENCES

Afkhami, S., & Bussmann, M. (2009). Height functions for applying contact angles to 3D VOF simulations. International journal for numerical methods in fluids, 61(8), 827-847.

Annapragada, S. R., Murthy, J. Y., & Garimella, S. V. (2012). Prediction of droplet dynamics on an incline. International Journal of Heat and Mass Transfer, 55(5), 1466-1474.

Barnes, G., & Gentle, I. (2011). Interfacial science: an introduction: Oxford University Press.

Berejnov, V., & Thorne, R. E. (2007). Effect of transient pinning on stability of drops sitting on an inclined plane. Physical Review E, 75(6), 066308.

Bhushan, B. (2011). Biomimetics inspired surfaces for drag reduction and oleophobicity/philicity. Beilstein journal of nanotechnology, 2(1), 66-84.

Bhushan, B., & Jung, Y. C. (2011). Natural and biomimetic artificial surfaces for superhydrophobicity, self-cleaning, low adhesion, and drag reduction. Progress in Materials Science, 56(1), 1-108.

Bhushan, B., Jung, Y. C., & Koch, K. (2009). Micro-, nano-and hierarchical structures for superhydrophobicity, self-cleaning and low adhesion. Philosophical Transactions of the Royal Society A: Mathematical, Physical and Engineering Sciences, 367(1894), 1631-1672.

Bico, J., Marzolin, C., & Quéré, D. (1999). Pearl drops. EPL (Europhysics Letters), 47(2), 220.

Bico, J., Thiele, U., & Quéré, D. (2002). Wetting of textured surfaces. Colloids and Surfaces A: Physicochemical and Engineering Aspects, 206(1), 41-46.

Bico, J., Tordeux, C., & Quéré, D. (2001). Rough wetting. EPL (Europhysics Letters), 55(2), 214.

Bisanda, E. (2000). The effect of alkali treatment on the adhesion characteristics of sisal fibres. Applied Composite Materials, 7(5-6), 331-339.

Bittoun, E., & Marmur, A. (2009). Optimizing super-hydrophobic surfaces: criteria for comparison of surface topographies. Journal of Adhesion Science and Technology, 23(3), 401-411.

Blossey, R. (2003). Self-cleaning surfaces—virtual realities. Nature materials, 2(5), 301-306.

Bommer, S., Scholl, H., Seemann, R., Kanhaiya, K., Sheraton M, V., & Verma, N. (2014). Depinning of drops on inclined smooth and topographic surfaces: Experimental and lattice Boltzmann model study. Langmuir, 30(37), 11086-11095.

Buick, J., & Greated, C. (2000). Gravity in a lattice Boltzmann model. Physical Review E, 61(5), 5307.

Callies, M., & Quéré, D. (2005). On water repellency. Soft matter, 1(1), 55-61.

Cassie, A., & Baxter, S. (1944). Wettability of porous surfaces. Transactions of the Faraday Society, 40, 546-551.

Chen, W., Fadeev, A. Y., Hsieh, M. C., Öner, D., Youngblood, J., & McCarthy, T. J. (1999). Ultrahydrophobic and ultralyophobic surfaces: some comments and examples. Langmuir, 15(10), 3395-3399.

Colosqui, C. E., Kavousanakis, M. E., Papathanasiou, A. G., & Kevrekidis, I. G. (2013). Mesoscopic model for microscale hydrodynamics and interfacial phenomena: Slip, films, and contact-angle hysteresis. Physical Review E, 87(1), 013302.

Davis, J. R. (2000). Corrosion: Understanding the basics: ASM International.

De Gennes, P.-G., Brochard-Wyart, F., & Quéré, D. (2004). Capillarity and wetting phenomena: drops, bubbles, pearls, waves: Springer Science & Business Media.

Dupuis, A., & Yeomans, J. (2005). Modeling droplets on superhydrophobic surfaces: equilibrium states and transitions. Langmuir, 21(6), 2624-2629.

Dupuis, A., & Yeomans, J. (2006). Dynamics of sliding drops on superhydrophobic surfaces. EPL (Europhysics Letters), 75(1), 105.

Dupuis, A., & Yeomans, J. M. (2004). Lattice Boltzmann modelling of droplets on chemically heterogeneous surfaces. Future Generation Computer Systems, 20(6), 993-1001.

Esmaili, E., Moosavi, A., & Mazloomi, A. (2012). The dynamics of wettability driven droplets in smooth and corrugated microchannels. Journal of Statistical Mechanics: Theory and Experiment, 2012(10), P10005.

Extrand, C. (2002). Model for contact angles and hysteresis on rough and ultraphobic surfaces. Langmuir, 18(21), 7991-7999.

Extrand, C. (2006). Designing for optimum liquid repellency. Langmuir, 22(4), 1711-1714.

Farhat, H. (2010). Accelerated Lattice Boltzmann Method For Colloidal Suspensions Rheology And Interface Morphology.

Fei, K., Cheng, C., & Hong, C. (2006). Lattice Boltzmann simulations of CO2 bubble dynamics at the anode of a μDMFC. Journal of fuel cell science and technology, 3(2), 180-187.

Feng, X., & Jiang, L. (2006). Design and creation of superwetting/antiwetting surfaces. Advanced Materials, 18(23), 3063-3078.

Fukai, J., Shiiba, Y., Yamamoto, T., Miyatake, O., Poulikakos, D., Megaridis, C., & Zhao, Z. (1995). Wetting effects on the spreading of a liquid droplet colliding with a flat surface: experiment and modeling. Physics of Fluids (1994-present), 7(2), 236-247.

Fukai, J., Zhao, Z., Poulikakos, D., Megaridis, C. M., & Miyatake, O. (1993). Modeling of the deformation of a liquid droplet impinging upon a flat surface. Physics of Fluids A: Fluid Dynamics (1989-1993), 5(11), 2588-2599.

Furmidge, C. (1962). Studies at phase interfaces. I. The sliding of liquid drops on solid surfaces and a theory for spray retention. Journal of colloid science, 17(4), 309-324.

Gao, L., & McCarthy, T. J. (2006). Contact angle hysteresis explained. Langmuir, 22(14), 6234-6237.

Genzer, J., & Efimenko, K. (2006). Recent developments in superhydrophobic surfaces and their relevance to marine fouling: a review. Biofouling, 22(5), 339-360.

Giese, R. F., & Van Oss, C. J. (2002). Colloid and surface properties of clays and related minerals (Vol. 105): CRC press.

Gong, S., & Cheng, P. (2012). Numerical investigation of droplet motion and coalescence by an improved lattice Boltzmann model for phase transitions and multiphase flows. Computers & Fluids, 53, 93-104.

Guo, Z., Liu, W., & Su, B.-L. (2011). Superhydrophobic surfaces: from natural to biomimetic to functional. Journal of colloid and interface science, 353(2), 335-355.

Gupta, P., Ulman, A., Fanfan, S., Korniakov, A., & Loos, K. (2005). Mixed self-assembled monolayers of alkanethiolates on ultrasmooth gold do not exhibit contact-angle hysteresis. Journal of the American Chemical Society, 127(1), 4-5.

Hao, L., & Cheng, P. (2009). Lattice Boltzmann simulations of liquid droplet dynamic behavior on a hydrophobic surface of a gas flow channel. Journal of Power Sources, 190(2), 435-446.

Harder, P. M., Shedd, T. A., & Colburn, M. (2008). Static and dynamic wetting characteristics of nano-patterned surfaces. Journal of Adhesion Science and Technology, 22(15), 1931-1948.

He, B., & Lee, J. (2003). Dynamic wettability switching by surface roughness effect. Paper presented at the Micro Electro Mechanical Systems, 2003. MEMS-03 Kyoto. IEEE The Sixteenth Annual International Conference on.

He, B., Patankar, N. A., & Lee, J. (2003). Multiple equilibrium droplet shapes and design criterion for rough hydrophobic surfaces. Langmuir, 19(12), 4999-5003.

Hollis, A., Spencer, T., Halliday, I., & Care, C. (2011). Dynamic wetting boundary condition for continuum hydrodynamics with multi-component lattice Boltzmann equation simulation method. IMA journal of applied mathematics, hxr008.

Hong, X., Gao, X., & Jiang, L. (2007). Application of superhydrophobic surface with high adhesive force in no lost transport of superparamagnetic microdroplet. Journal of the American Chemical Society, 129(6), 1478-1479.

Huang, J., Shu, C., & Chew, Y. (2008). Numerical investigation of transporting droplets by spatiotemporally controlling substrate wettability. Journal of colloid and interface science, 328(1), 124-133.

Hyväluoma, J., Koponen, A., Raiskinmäki, P., & Timonen, J. (2007). Droplets on inclined rough surfaces. The European Physical Journal E: Soft Matter and Biological Physics, 23(3), 289-293.

Inamuro, T., Ogata, T., Tajima, S., & Konishi, N. (2004). A lattice Boltzmann method for incompressible two-phase flows with large density differences. Journal of Computational Physics, 198(2), 628-644.

Kamusewitz, H., Possart, W., & Paul, D. (1999). The relation between Young's equilibrium contact angle and the hysteresis on rough paraffin wax surfaces. Colloids and Surfaces A: Physicochemical and Engineering Aspects, 156(1), 271-279.

Kang, Q., Zhang, D., & Chen, S. (2005). Displacement of a three-dimensional immiscible droplet in a duct. Journal of Fluid Mechanics, 545, 41-66.

Kim, S. H. (2008). Fabrication of superhydrophobic surfaces. Journal of Adhesion Science and Technology, 22(3-4), 235-250.

Kim, Y. H., Choi, W., & Lee, J. S. (2011). Water droplet properties on periodically structured superhydrophobic surfaces: a lattice Boltzmann approach to multiphase flows with high water/air density ratio. Microfluidics and Nanofluidics, 10(1), 173-185.

Koch, G. H., Brongers, M. P., Thompson, N. G., Virmani, Y. P., & Payer, J. H. (2002). Corrosion cost and preventive strategies in the United States.

Kwon, H.-M., Paxson, A. T., Varanasi, K. K., & Patankar, N. A. (2011). Rapid deceleration-driven wetting transition during pendant drop deposition on superhydrophobic surfaces. Physical review letters, 106(3), 036102.

Lafuma, A., & Quéré, D. (2003). Superhydrophobic states. Nature materials, 2(7), 457-460.

Latva-Kokko, M., & Rothman, D. H. (2005). Static contact angle in lattice Boltzmann models of immiscible fluids. Physical Review E, 72(4), 046701.

Léopoldés, J., Dupuis, A., Bucknall, D., & Yeomans, J. (2003). Jetting micron-scale droplets onto chemically heterogeneous surfaces. Langmuir, 19(23), 9818-9822.

Li, W., Wang, X., Chen, Z., Waje, M., & Yan, Y. (2005). Carbon nanotube film by filtration as cathode catalyst support for proton-exchange membrane fuel cell. Langmuir, 21(21), 9386-9389.

Lifton, V. A., Simon, S., & Frahm, R. E. (2005). Reserve battery architecture based on superhydrophobic nanostructured surfaces. Bell Labs Technical Journal, 10(3), 81-85.

Lister, J., Morrison, N., & Rallison, J. (2006). Sedimentation of a two-dimensional drop towards a rigid horizontal plane. Journal of Fluid Mechanics, 552, 345-351.

Lu, C., Xie, Y., Yang, Y., Cheng, M. M.-C., Koh, C.-G., Bai, Y., Juang, Y.-J. (2007). New valve and bonding designs for microfluidic biochips containing proteins. Analytical chemistry, 79(3), 994-1001.

Lv, C., Yang, C., Hao, P., He, F., & Zheng, Q. (2010). Sliding of water droplets on microstructured hydrophobic surfaces. Langmuir, 26(11), 8704-8708.

Ma, M., & Hill, R. M. (2006). Superhydrophobic surfaces. Current opinion in colloid & interface science, 11(4), 193-202.

Macdougall, G., & Ockrent, C. (1942). Surface energy relations in liquid/solid systems. I. The adhesion of liquids to solids and a new method of determining the surface tension of liquids. Proceedings of the Royal Society of London. Series A. Mathematical and Physical Sciences, 180(981), 151-173.

Marmur, A. (2003). Wetting on hydrophobic rough surfaces: to be heterogeneous or not to be? Langmuir, 19(20), 8343-8348.

Marmur, A. (2004). The lotus effect: superhydrophobicity and metastability. Langmuir, 20(9), 3517-3519.

Martines, E., Seunarine, K., Morgan, H., Gadegaard, N., Wilkinson, C. D., & Riehle, M. O. (2005). Superhydrophobicity and superhydrophilicity of regular nanopatterns. Nano letters, 5(10), 2097-2103.

Martys, N. S., & Chen, H. (1996). Simulation of multicomponent fluids in complex three-dimensional geometries by the lattice Boltzmann method. Phys Rev E Stat Phys Plasmas Fluids Relat Interdiscip Topics, 53(1), 743-750.

McHale, G., Shirtcliffe, N., & Newton, M. (2004). Contact-angle hysteresis on super-hydrophobic surfaces. Langmuir, 20(23), 10146-10149.

McHale, G., Shirtcliffe, N. J., Aqil, S., Perry, C. C., & Newton, M. I. (2004). Topography driven spreading. Physical review letters, 93(3), 036102.

Milne, A., & Amirfazli, A. (2012). The Cassie equation: How it is meant to be used. Advances in colloid and interface science, 170(1), 48-55.

Miwa, M., Nakajima, A., Fujishima, A., Hashimoto, K., & Watanabe, T. (2000). Effects of the surface roughness on sliding angles of water droplets on superhydrophobic surfaces. Langmuir, 16(13), 5754-5760.

Mo, G. C., Liu, W.-y., & Kwok, D. Y. (2005). Surface-ascension of discrete liquid drops via experimental reactive wetting and lattice Boltzmann simulation. Langmuir, 21(13), 5777-5782.

Neinhuis, C., & Barthlott, W. (1997). Characterization and distribution of water-repellent, self-cleaning plant surfaces. Annals of Botany, 79(6), 667-677.

Nosonovsky, M. (2007). On the range of applicability of the Wenzel and Cassie equations. Langmuir, 23(19), 9919-9920.

Nosonovsky, M., & Bhushan, B. Green tribology: biomimetics, energy conservation, and sustainability, 2012: Springer.

Nosonovsky, M., & Bhushan, B. (2005). Roughness optimization for biomimetic superhydrophobic surfaces. Microsystem Technologies, 11(7), 535-549.

Nosonovsky, M., & Bhushan, B. (2007). Hierarchical roughness optimization for biomimetic superhydrophobic surfaces. Ultramicroscopy, 107(10), 969-979.

Okiishi, M. Y., Munson, B., & Young, D. (2006). Fundamentals of Fluid Mechanics. John Wiley & Sons, Inc.

Onda, T., Shibuichi, S., Satoh, N., & Tsujii, K. (1996). Super-water-repellent fractal surfaces. Langmuir, 12(9), 2125-2127.

Öner, D., & McCarthy, T. J. (2000). Ultrahydrophobic surfaces. Effects of topography length scales on wettability. Langmuir, 16(20), 7777-7782.

Ou, J., Perot, B., & Rothstein, J. P. (2004). Laminar drag reduction in microchannels using ultrahydrophobic surfaces. Physics of Fluids (1994-present), 16(12), 4635-4643.

Patankar, N. A. (2003). On the modeling of hydrophobic contact angles on rough surfaces. Langmuir, 19(4), 1249-1253.

Patankar, N. A. (2004). Mimicking the lotus effect: influence of double roughness structures and slender pillars. Langmuir, 20(19), 8209-8213.

Patankar, N. A. (2004). Transition between superhydrophobic states on rough surfaces. Langmuir, 20(17), 7097-7102.

Patankar, N. A. (2009). Hydrophobicity of surfaces with cavities: making hydrophobic substrates from hydrophilic materials? Journal of Adhesion Science and Technology, 23(3), 413-433.

Patankar, N. A. (2010). Consolidation of hydrophobic transition criteria by using an approximate energy minimization approach. Langmuir, 26(11), 8941-8945.

Pericet-Cámara, R., Best, A., Butt, H.-J. r., & Bonaccurso, E. (2008). Effect of capillary pressure and surface tension on the deformation of elastic surfaces by sessile liquid microdrops: An experimental investigation. Langmuir, 24(19), 10565-10568.

Petrie, R. J., Bailey, T., Gorman, C. B., & Genzer, J. (2004). Fast directed motion of “Fakir” droplets. Langmuir, 20(23), 9893-9896.

Quéré, D. (2002). Rough ideas on wetting. Physica A: Statistical Mechanics and its Applications, 313(1), 32-46.

Quéré, D. (2008). Wetting and roughness. Annu. Rev. Mater. Res., 38, 71-99.

Raiskinmäki, P., Koponen, A., Merikoski, J., & Timonen, J. (2000). Spreading dynamics of three-dimensional droplets by the lattice-Boltzmann method. Computational Materials Science, 18(1), 7-12.

Raj, R., Enright, R., Zhu, Y., Adera, S., & Wang, E. N. (2012). Unified model for contact angle hysteresis on heterogeneous and superhydrophobic surfaces. Langmuir, 28(45), 15777-15788.

Richard, D. (1999). Viscous drops rolling on a tilted non-wettable solid. EPL (Europhysics Letters), 48(3), 286.

Rios, P., Dodiuk, H., Kenig, S., McCarthy, S., & Dotan, A. (2008). Durable ultra-hydrophobic surfaces for self-cleaning applications. Polymers for Advanced Technologies, 19(11), 1684-1691.

Sakai, M., Hashimoto, A., Yoshida, N., Suzuki, S., Kameshima, Y., & Nakajima, A. (2007). Image analysis system for evaluating sliding behavior of a liquid droplet on a hydrophobic surface. Review of scientific instruments, 78(4), 045103.

Sakai, M., Song, J.-H., Yoshida, N., Suzuki, S., Kameshima, Y., & Nakajima, A. (2006). Direct observation of internal fluidity in a water droplet during sliding on hydrophobic surfaces. Langmuir, 22(11), 4906-4909.

Sakai, M., Song, J.-H., Yoshida, N., Suzuki, S., Kameshima, Y., & Nakajima, A. (2006). Relationship between sliding acceleration of water droplets and dynamic contact angles on hydrophobic surfaces. Surface science, 600(16), L204-L208.

Sandre, O., Gorre-Talini, L., Ajdari, A., Prost, J., & Silberzan, P. (1999). Moving droplets on asymmetrically structured surfaces. Physical Review E, 60(3), 2964.

Sbragaglia, M., Benzi, R., Biferale, L., Succi, S., & Toschi, F. (2006). Surface roughness-hydrophobicity coupling in microchannel and nanochannel flows. Physical review letters, 97(20), 204503.

Schmieschek, S., & Harting, J. (2009). Contact angle determination in multicomponent lattice Boltzmann simulations. arXiv preprint arXiv:0910.3915.

Shan, X., & Chen, H. (1993). Lattice Boltzmann model for simulating flows with multiple phases and components. Physical Review E, 47(3), 1815.

Shirtcliffe, N. J., Aqil, S., Evans, C., McHale, G., Newton, M. I., Perry, C. C., & Roach, P. (2004). The use of high aspect ratio photoresist (SU-8) for super-hydrophobic pattern prototyping. Journal of Micromechanics and Microengineering, 14(10), 1384.

Stensholt, S., & Øien, A. (2011). Lattice Boltzmann simulations of the motion induced by variable surface tension. Advances in Engineering Software, 42(11), 944-953.

Suzuki, S., Sakai, M., Yoshida, N., Hashimoto, A., Kameshima, Y., Okada, K., & Nakajima, A. (2010). Sliding Behavior of Water Droplets on Smooth Hydrophobic Fluoroalkylsilane Coatings with Different Surface Coverage Ratio. Shikizai kyokaishi, 83(12), 499-504.

Trapaga, G., Matthys, E., Valencia, J., & Szekely, J. (1992). Fluid flow, heat transfer, and solidification of molten metal droplets impinging on substrates: comparison of numerical and experimental results. Metallurgical Transactions B, 23(6), 701-718.

Trapaga, G., & Szekely, J. (1991). Mathematical modeling of the isothermal impingement of liquid droplets in spraying processes. Metallurgical Transactions B, 22(6), 901-914.

van Kats, F. M., & Egberts, P. J. (1998). Spreading dynamics modeled by Lattice–Boltzmann techniques. Journal of colloid and interface science, 205(1), 166-177.

Vanapalli, S. A., Banpurkar, A. G., van den Ende, D., Duits, M. H., & Mugele, F. (2009). Hydrodynamic resistance of single confined moving drops in rectangular microchannels. Lab on a Chip, 9(7), 982-990.

Varnik, F., Dorner, D., & Raabe, D. (2007). Roughness-induced flow instability: a lattice Boltzmann study. Journal of Fluid Mechanics, 573, 191-209.

Wang, L., Huang, H.-b., & Lu, X.-Y. (2013). Scheme for contact angle and its hysteresis in a multiphase lattice Boltzmann method. Physical Review E, 87(1), 013301.

Watanabe, K., Udagawa, Y., & Udagawa, H. (1999). Drag reduction of Newtonian fluid in a circular pipe with a highly water-repellent wall. Journal of Fluid Mechanics, 381, 225-238.

Wenzel, R. N. (1936). Resistance of solid surfaces to wetting by water. Industrial & Engineering Chemistry, 28(8), 988-994.

White, F. M., & Corfield, I. (2006). Viscous fluid flow (Vol. 3): McGraw-Hill New York.

Whyman, G., Bormashenko, E., & Stein, T. (2008). The rigorous derivation of Young, Cassie–Baxter and Wenzel equations and the analysis of the contact angle hysteresis phenomenon. Chemical Physics Letters, 450(4), 355-359.

Wier, K. A., & McCarthy, T. J. (2006). Condensation on ultrahydrophobic surfaces and its effect on droplet mobility: ultrahydrophobic surfaces are not always water repellant. Langmuir, 22(6), 2433-2436.

Wu, J., Xia, J., Lei, W., & Wang, B.-p. (2014). Pinning mechanism of advancing sessile droplet on superhydrophobic surfaces. RSC Advances, 4(67), 35649-35652.

Yagub A., Farhat H., Kondaraju S., Singh T. (2015) A Lattice Boltzmann Model for Substrates with Regularly Structured Surface Roughness. Journal of Computational Physics. Received 6 October 2014, Revised 4 July 2015, Accepted 30 August 2015, Available online 3 September 2015.

Yan, Y., & Zu, Y. (2007). A lattice Boltzmann method for incompressible two-phase flows on partial wetting surface with large density ratio. Journal of Computational Physics, 227(1), 763-775.

Yang, J.-T., Chen, J. C., Huang, K.-J., & Yeh, J. A. (2006). Droplet manipulation on a hydrophobic textured surface with roughened patterns. Microelectromechanical Systems, Journal of, 15(3), 697-707.

Yoshimitsu, Z., Nakajima, A., Watanabe, T., & Hashimoto, K. (2002). Effects of surface structure on the hydrophobicity and sliding behavior of water droplets. Langmuir, 18(15), 5818-5822.

Youngblood, J. P., & McCarthy, T. J. (1999). Ultrahydrophobic polymer surfaces prepared by simultaneous ablation of polypropylene and sputtering of poly (tetrafluoroethylene) using radio frequency plasma. Macromolecules, 32(20), 6800-6806.

Yu, D., Mei, R., & Shyy, W. (2002). A multi-block lattice Boltzmann method for viscous fluid flows. International journal for numerical methods in fluids, 39(2), 99-120.

Zhang, J., & Kwok, D. Y. (2006). Contact line and contact angle dynamics in superhydrophobic channels. Langmuir, 22(11), 4998-5004.

Zhang, X., Shi, F., Niu, J., Jiang, Y., & Wang, Z. (2008). Superhydrophobic surfaces: from structural control to functional application. Journal of Materials Chemistry, 18(6), 621-633.

Zhao, H., Park, K.-C., & Law, K.-Y. (2012). Effect of surface texturing on superoleophobicity, contact angle hysteresis, and “robustness”. Langmuir, 28(42), 14925-14934.

Zheng, L., & Zhang, H. (2000). An adaptive level set method for moving-boundary problems: application to droplet spreading and solidification. Numerical Heat Transfer: Part B: Fundamentals, 37(4), 437-454.

Zhu, L., Feng, Y., Ye, X., & Zhou, Z. (2006). Tuning wettability and getting superhydrophobic surface by controlling surface roughness with well-designed microstructures. Sensors and Actuators A: Physical, 130, 595-600.

ABSTRACT

SPECIALIZED INTER-PARTICLE INTERACTION LBM FOR PATTERNED SUPERHYDROPHOBIC SURFACES

by

AMAL S. YAGUB

December 2015

Advisor: Dr. Trilochan Singh

Co-Advisor: Dr. Hassan Farhat

Major: Mechanical Engineering

Degree: Doctor of Philosophy

Superhydrophobic surface characteristics are important in many industrial applications, ranging from the textile to the military. It was observed that surfaces fabricated with nano/micro roughness can manipulate the droplet contact angle, thus providing an opportunity to control the droplet wetting characteristics. The Shan and Chen (SC) lattice Boltzmann model (LBM) is a good numerical tool, which holds strong potentials to qualify for simulating droplets wettability. This is due to its realistic nature of droplet contact angle (CA) prediction on flat smooth surfaces. But SC-LBM was not able to replicate the CA on rough surfaces because it lacks a real representation of the physics at work under these conditions. By using a correction factor to influence the interfacial tension within the asperities, the physical forces acting on the droplet at its contact lines were mimicked. This approach allowed the model to replicate some experimentally confirmed Wenzel and Cassie wetting cases. Regular roughness structures with different spacing were used to validate the study using the classical Wenzel and Cassie equations. This work highlights the strength and weakness of the SC model and attempts to

qualitatively conform it to the fundamental physics, which causes a change in the droplet apparent contact angle, when placed on nano/micro structured surfaces.

In the second part of this work, the model is used also to analyze the sliding of droplets in contact with flat horizontal surfaces. This part identifies the main factors, which influence the multiphase fluids transport in squared channels. Effects of dimensionless radius, Weber number, Reynolds number and static contact angles are evaluated by calculating the power required for moving single droplets in comparison to the power needed for moving the undisturbed flow in the channel. Guidelines for optimizing the design of such flow are presented.

In last part of work, the sliding of droplets on sloped surfaces with and without roughness is numerically investigated. The Shan and Chen (SC) Lattice Boltzmann model (LBM) is used to analyze the effect of pinning on the movement of droplets placed on sloped surfaces. The model is checked for conformance with the Furmidge equation which applies to tilted unstructured surfaces. It is shown that a droplet sliding on a perfectly smooth surface requires very minimal slope angle and that pinning due to the inhomogeneous nature of manufactured smooth surfaces is the key factor in determining the minimal slope angle. The model is also used on sloped rough surfaces to check the effects of roughness on the movement of single droplets. The numerical outcomes are compared with published experimental results for validation and a dimensionless number is suggested for quantifying the degree of pinning needed to control the behavior of sliding droplets on sloped surfaces.

AUTOBIOGRAPHICAL STATEMENT

AMAL S. YAGUB

EDUCATION:

- PhD Mechanical Engineering, Wayne State University, Detroit, Michigan USA
- M.Sc. Mechanical Engineering, Wayne State University, Detroit, Michigan USA
- Alternative Energy Technology Graduate Certificate, WSU, Detroit, Michigan USA
- M.Sc. Aeronautical Engineering, Al-Fateh University, Tripoli, Libya
- B.Sc. Aeronautical Engineering, Al-Fateh University, Tripoli, Libya

EXPERIENCE:

-Researcher Engineer, Wind Energy Dept.–Solar Energy Research Center, Tripoli, Libya (1996 – 2008)

PUBLICATIONS:

-Yagub A., Farhat H., Kondaraju S., Singh T., “A Lattice Boltzmann Model for Substrates with Regularly Structured Surface Roughness”. Journal of Computational Physics 301 (2015) 402–414

-Yagub A., Farhat H., Kondaraju S., Singh T. “Lattice Boltzmann Simulations for Disturbed Parabolic Flows with Single Droplet on Smooth Planes and on Surfaces with Squared Roughness”. (in progress)

-Yagub A., Hassan W., Farhat H., Kondaraju S., Singh T. **.**Lattice Boltzmann Method for Single Sliding Droplets on sloped Flat and Rough Surfaces. (in progress).